Seismic history from in situ 36Cl cosmogenic nuclide data on limestone fault scarps using Bayesian reversible jump Markov chain Monte Carlo

J. Tesson, Lucilla Benedetti, Jump Markov, Monte Carlo

Seismic history from in situ ^{36}Cl cosmogenic nuclide data on limestone fault scarps using Bayesian Reversible Jump Markov chain Monte Carlo

Tesson J.[1] and Benedetti L.[1]

[1] *Aix-Marseille Université, CEREGE CNRS-IRD UMR 34, Aix en Provence, France*

Corresponding author: *J. Tesson, Aix-Marseille Université CEREGE CNRS-IRD UMR 34, Plateau de l'Arbois, Aix en Provence, 13545, France. (jim.tesson@gmail.com)*

Abstract

Constraining the past seismic activity and the slip-rates of faults over several millennials is crucial for seismic hazard assessment. Chlorine 36 (^{36}Cl) in situ produced cosmogenic nuclide is increasingly used to retrieve past earthquakes histories on seismically exhumed limestone normal fault-scarps. Here we present a new methodology to retrieve the exhumation history based on a Bayesian transdimensional inversion of the ^{36}Cl data and using the latest muon production calculation method. This procedure uses the reversible jump Markov chains Monte-Carlo algorithm (RJ-MCMC, Green 1995) which enables 1-exploring the parameter space (number of events, age and slip of the events), 2-finding the most probable scenarios, and 3- quantifying the associated uncertainties. Through a series of synthetic tests, the algorithm revealed a great capacity to constrain event slips and ages in a short computational time (several days) with a precision that can reach 0.1 ky and 0.5 m for the age and slip of exhumation event, respectively. In addition, our study show that the amount of ^{36}Cl accumulated when the sampled fault-plane was still buried under the colluvial wedge, prior its exhumation, might represents up to 35 % of the total ^{36}Cl. Additional sampling under the colluvial is necessary to constrain this contribution.

Introduction

Active normal faults in carbonated environments often produced continuous 1-20 m high bedrock fault scarp as the result of one-to-several earthquake displacements on the fault plane. This has been recently well illustrated during the 30/10/16 Amatrice earthquake of Mw=6.5 that triggered an exhumation of 1 to 2 m of the base of the limestone fault scarp

along at least 7 km (see Fig. 1) (Villani et al. 2018, Perouse et al. 2018). When those morphological features are preserved from natural and anthropogenic degradation, they can be used as a marker of paleo-earthquakes allowing recovering crucial information about the timing and the magnitude of the past large earthquakes. Few studies have proposed to assess the amplitude of the past slip events using the morphology of the fault plane surface. In particular, the presence of horizontal bands of lighter color on some fault planes visible on aerial pictures and/or backscattered electromagnetic signals, or the brutal end of vertical karstic weathering features (flutes) on some fault planes have suggested that they might represent paleo–interface between the exhumed fault plane and the colluvium soil, that have been uplifted because of earthquakes (Giaccio et al., 2012; Wiatr et al., 2015). Recently, high-resolution digital elevation models of the exhumed fault plane of the Pisia fault (Greece) revealed a vertical variability of the roughness along the fault plane, with peaks delimiting deci-to-decametric horizontal bands (Wiatr et al., 2015; He et al., 2016). Those studies thus suggest that the exhumation process producing the fault-plane, or its exposure history since exhumation might be able to partially control its physical properties. On the other hand, the systematic chemical analysis of the carbonated bedrock fault plane along vertical profiles has revealed that the concentration of the in situ produced cosmogenic nuclide 36-Chlorine (^{36}Cl) and the concentration of the rare earth elements (REE) are highly modulated by the exhumation process (Carcaillet et al., 2008). The approach based on the measured content of in-situ produced ^{36}Cl has provided an unique opportunity to determine both the slip of the past large earthquakes, and to date those events (Mitchell et al., 2001; Benedetti et al., 2002; Schlagenhauf et al., 2010). The REE content analysis has improved our capacity to distinguish slip events because the buildup kinematic appears to be faster than the ^{36}Cl in situ production (Carcaillet et al., 2008; Tesson et al., 2016).

At the same time, the thorough analysis of the fault-scarp geometry and of the colluvial wedge sub-surface morphology by means of field observations and geophysical investigations (Lidar, GPR) have proven to be essential to assess the origin of the fault plane exhumation (Schlagenhauf et al., 2010; Giaccio et al., 2012; Bubeck et al., 2015; Wilkinson et al., 2015). For instance, erosion of the fault scarp by collapsed of unconsolidated portion of the scarp, fluvial erosion due to drainage crossing the fault or anthropogenic modifications can modify the exhumation chronology, avoiding reliable results on the seismic exhumation history.

So far, the only possibility to date the exhumation of a carbonated fault plane is to use the ^{36}Cl cosmogenic nuclide which results from the interaction of cosmic rays and mainly the Calcium contained in carbonate rocks. Determining the ^{36}Cl concentration ($[^{36}Cl]$) of rock samples collected on a fault-plane surface thus potentially enables to date the different exhumational phases of the fault plane and quantify the amplitude of each slip events (Benedetti et al., 2002; Mitchell et al., 2001). Because cosmic rays are able to penetrate up to 4-10 m depth below the ground surface (Gosse and Phillips, 2001; Schlagenhauf, 2010), a today-exhumed fault plane has firstly accumulated ^{36}Cl at depth when buried below the colluvium, and secondly when exhumed and directly exposed to cosmic rays (Schlagenhauf et al., 2010). The exhumation age of a sample belonging to the fault plane surface thus requires integrating its whole exhumation history from depth to surface, that is modulated by the number of events, their displacements and ages. Several pioneering studies applied the equations describing the cosmogenic production to such dynamic surface providing a way to precisely calculate the vertical synthetic $[^{36}Cl]$ profile that should be observed on a fault-plane for a given exhumation scenario (Mitchell et al., 2001; Benedetti et al., 2002, 2003; Schlagenhauf et al., 2010). Over the last five years, more than a dozen of seismic histories have been inferred from ^{36}Cl cosmogenic dating of seismically exhumed fault plane (Schlagenhauf et al., 2011; Akçar et al., 2012; Benedetti et al., 2013; Mouslopoulou et al., 2014; Tesson et al., 2016; Cowie et al., 2017) all using the latest published methodology (Schlagenhauf et al., 2010). More recently, Beck et al. (2018) published a new modelling code, built upon the Schlagenhauf et al. (2010) code with an inversion procedure. Here we present a new inversion procedure (called Modelscarp inversion) using a Reversible Jump Markov chain Monte Carlo (RJ-McMC, Green, 1995; Gallagher et al., 2011; Sambridge, 2012), in which we include the full ^{36}Cl build-up of a fault scarp with in particular an updated muon production rate calculation. We show through synthetic tests that our modelling is able to decipher with great accuracy complex scenario including seismic clusters and quiescence periods, and that accounting for the slip history prior to the post-glacial exhumation is crucial. The code and a complete tutorial are released in the present article (https://github.com/jimtesson/Modelscarp_Inversion).

I. Recovering past earthquakes from a ^{36}Cl profile

1. Formation and preservation of normal fault-scarp

Many authors attribute the persistence of limestone bedrock fault-scarp along normal faults to be the direct consequence of climatic condition changes in the Mediterranean that occurred at the end of the last glacial maximum period (Armijo et al., 1992; Giraudi and Frezzotti, 1995; Piccardi et al., 1999). This major climatic change from cold glacial to warmer inter-glacial conditions apparently resulted in an abrupt decrease of the hill-slope erosion rate and a general stabilization of mountain slopes by the vegetation as suggested by several records in continental lakes showing a drastic decrease of clastic input and an increase of terrestrial vegetation (Giaccio et al., 2015). This environmental modification has led to preserve the vertical offset produced by normal faulting over the last 16-20 kyr (Armijo et al., 1992; Giraudi and Frezzotti, 1997; Piccardi et al., 1999; Tucker et al., 2011). Hence, the 1-20 m high steep scarp commonly observed along active normal faults (Fig. 2) have long been interpreted as being the cumulative vertical offset caused by multiple co-seismic displacement on the fault plane over the last 18 ka (hereinafter referred as the "post-glacial" fault-scarp). Those preserved fault-scarps are usually topped by a relatively smooth and gentle 10-40° dipping surface (hereinafter referred as the "peri-glacial surface", Fig 2), representing the older exhumed footwall, that has progressively retreated from the fault plane due to the long-term abrasion that occurred during peri-glacial period (Tucker et al., 2011). During those periods of enhanced erosion, a significant amount of sediments is deposited on the hanging-wall compartment of the fault, forming a colluvial wedge at the base of the fault plane (Fig. 2). Schlagenhauf et al. (2011) dated with radiocarbon dating two charcoal found in the colluvial wedge of the Magnola fault scarp at 31.6 ± 0.5 and 38.8 ± 1.2 ka BP. Those ages are in agreement with the assumption that the colluvial wedge has been deposited during the Pleistocene.

2. ^{36}Cl build-up in an exhumed fault plane

(i) ^{36}Cl accumulation in the fault-plane

The ^{36}Cl accumulation within a rock sample belonging to a fault-plane have been formalized by Schlagenhauf et al. (2010). The model includes various factors that modulate the ^{36}Cl production rate within the rock, such as the site location, the

shielding resulting from the geometry of the fault-scarp and associated colluvium, the scarp denudation, the chemical composition of the fault-plane rock and of the colluvial wedge, the geomagnetic field temporal variations, and the possible snow cover.

Basically, in absence of denudation, the concentration of ^{36}Cl in a rock varies as a function of rock exposure time (t) and burial depth (z), as

$$dN(z,t)/dt = P_{36Cl}(z,t) - \lambda \times N(z,t) \quad \text{Eq. (1)}$$

where N is the number of atoms of ^{36}Cl, P_{36Cl} is the ^{36}Cl isotope production rate, λ is the decay constant of ^{36}Cl, and dN /dt is the rate of change.

According to Schlagenhauf et al. 2010, the total ^{36} Cl production rate for a preserved rock sample (i.e. sustaining no denudation) of a normal fault scarp, close to the ground surface, can be calculated:

$$P_{36Cl}(\mathrm{z,t}) = P(z) \times S(t) \times F(z) \times Q + P_{rad} \quad \text{Eq. (2)}$$

P(z) is the sample-specific ^{36}Cl production rate modulated by the sample chemical composition and the sample depth, and P_{rad} is the radiogenic production. *S*, *F* and *Q* are scaling factors: *S* accounts for elevation, latitude and geomagnetic field (may vary over the time), *F* accounts for the corrections related to shielding effects (topographic, geometric and cover shielding) and may varies with sample position along the fault-plane, and *Q* accounts for the sample thickness.

As shown by the equation (2), the amount of ^{36}Cl in a sample of the fault-plane is thus controlled by its position *z* (exhumed or buried) along the fault-plane, and by the time. The amount of ^{36}Cl in a sample thus integrates its whole history of exhumation, i.e. its successive positions z_i over the time, and the time periods T_i during which the sample has remained at each position z_i. In fine, the successive positions z_i are directly controlled by the amplitude of each slip event, while the time periods T_i corresponds to the inter-event time between two slip event. Determining the exhumation history of a fault-plane from its ^{36}Cl content means resolving the successive position Zi of each sample over the time.

The amount of ^{36}Cl accumulated in a today-exhumed fault plane can be presented as the sum of two contributions: a first contribution corresponding to the amount of ^{36}Cl accumulated at depth when buried under the colluvium during the **peri-glacial periods** (> 18 ka), hereinafter called the inherited contribution ($N^{36}Cl_{inherited}$), and a second contribution that accounts for the ^{36}Cl accumulated during the **post-glacial exhumation** of the fault-plane ($N^{36}Cl_{PG}$). The final amount of ^{36}Cl within each sample (i) is thus the sum of those two contributions (Eq. 1):

$$N^{36}Cl_{final}(i) = N^{36}Cl_{inherited}(i) + N^{36}Cl_{PG}(i) \quad \text{Eq. (3)}$$

The modeling of the ^{36}Cl accumulated within the fault plane during those two distinct periods is explained in the following section.

(ii) Inherited ^{36}Cl contribution

The initial conditions for the model are driven by the rate at which a footwall sample is approaching the surface. We assume two cases to model this rate.

In the first case the normal fault has been slipping for a long-time period (> 50-100 kyr), which is attested by a long-term morphology (i.e. 100-300 m high topographic scarp, presence of facet spur, strong incised gullies, perched valley (such as the Sparta fault in Greece or the Magnola fault in Italy ; Benedetti et al., (2002); Palumbo et al., (2004)) (Fig. 3-A). The inherited contribution is parameterized by the term "slip-rate of the fault", further called "peri-glacial fault slip-rate" that directly controls the successive position Z_i of each sample over the time.

This ^{36}Cl contribution is numerically resolved for each sample of the fault plane by predicting the position $z_i(t)$ over the time (Eq. 4). Samples are artificially placed at greater depth where the production rate of ^{36}Cl is null, and progressively raise towards the surface according to the peri-glacial fault slip-rate (*SR*), finally reaching their position just before the post-glacial exhumation history starts. At each time step *dt* (=100 yr), *z(t)* is moves upward according to the peri-glacial fault slip-rate:

$$z(t_i) = z(t_{i-1}) + SR * dt \quad \text{Eq. (4)}$$

The inherited ^{36}Cl ($N\,^{36}Cl_{\,inherited}$) within each sample is computed as the integral of the ^{36}Cl accumulated over the duration of the inherited period:

$$N\,^{36}Cl_{\,inherited} = \int_{0}^{300\,kyr} P_{36Cl}(z(t)) \times \frac{\left(1 - e^{-\lambda dt}\right)}{\lambda} \qquad \text{Eq. (5)}$$

where $N\,^{36}Cl_{\,inherited}$ is the theoretical number of atoms of ^{36}Cl accumulated in the sample during the rise of the sample, P_{36Cl} is the ^{36}Cl production rate within each sample depending on the depth of the sample z, λ is the decay constant of the ^{36}Cl, and t is the time since the fault started to slip. The duration of the long-term rise can be evaluated from the height of the long-term topographical scarp at each site and assuming an *a priori* peri-glacial slip-rate (Fig. 3-A). For instance, a cumulative fault scarp of 300 m high produced by a fault slipping at 1 mm/yr would give a maximum duration of 300 kyr.

In the second case, the fault has not been active in the past, or its slip-rate was very low. The erosional processes mainly control the overall morphology of the scarp (Fig. 3-B), with no long-term topographical scarp and a low dipping peri-glacial abrasion surface (<10°), as observed for example at the Nahef fault (Israel, Mitchell et al., (2001)), the Kaparelli fault (Benedetti et al., (2003), or the Fiamignano fault (Bubeck et al. 2015)). In that case, the inherited ^{36}Cl contribution is directly controlled by the denudation rate, the surface is at steady state prior exhumation (Fig. 3-B). In such case, the inherited ^{36}Cl is also parameterized using Eq. 5, i.e. samples are artificially placed at greater depth where the production rate of ^{36}Cl is null, and progressively raise towards the surface according to the long-term (or peri-glacial) denudation-rate (ε). Since the ^{36}Cl production originating from muons might be important at depth (Balco, 2017; Braucher et al., 2011), the inherited contribution can account for a significant proportion of the total measured ^{36}Cl in the sample, and has to be considered.

———

(iii) ^{36}Cl contribution from Post-glacial exhumation (< 20 kyr ago)

When warmer conditions are renewed, the fault plane is progressively exhumed from below the colluvium by successive earthquakes and preserved until today because of low erosion-rate and low supply of sediments preventing the fault plane from being dismantled or buried. Calculating the ^{36}Cl build up on a sample from the fault plane during the post-glacial period consists in resolving the successive positions *z(t)* of the sample over time, which modulates the ^{36}Cl production rate (see Eq. 2). After each event *n*, the depth position of the sample is updated as a function of its position prior to the event ($z_{Ev\,n-1}$), and the event displacement ($Slip_{Ev\,n}$):

$$z_{Ev\,n} = z_{Ev\,n-1} + Slip_{Ev\,n} \qquad \text{Eq. (6)}$$

The ^{36}Cl production rate is thus controlled by the displacement of each slip event that directly modifies the depth position of the sample. The time period during which the sample has remained at each position *z* and has accumulated ^{36}Cl is controlled by the time between each event.

In our model, the ^{36}Cl accumulated during the post-glacial period is thus parameterized by a given number of slip events, by their displacements, and by their ages. Those parameters enable to calculate the successive position of a sample and thus its ^{36}Cl production rate over the time. The post-glacial ^{36}Cl contribution is computed within each sample as being the sum of the ^{36}Cl accumulated between each event (Eq. 7):

$$N^{36}Cl_{PG} = \sum_{n=1}^{n_{EQmax}} P(z_{Ev\,n}) \times \frac{\left(1 - e^{-\lambda \times T_{n \to n+1}}\right)}{\lambda} \qquad \text{Eq. (7)}$$

Where $N^{36}Cl_{PG}$ is the theoretical number of atoms of ^{36}Cl accumulated in the sample during the post-glacial period, *n* is the index of each earthquake, n_{EQmax} is the total number of earthquakes that exhumed the sampled fault-plane, $z_{ev\,n}$ is the sample depth position of the sample along the fault-plane after the *n* event, $P(z_{Eq\,n})$ is the production rate within the sample for the given $z_{ev\,n}$ position, and $T_{n \to n+1}$ is the time period between two successive events *n* and *n+1*,

The uppermost and older section of the fault plane is often less well preserved, with diffusion-shape profile toward the peri-glacial abrasion surface. Large fractures, pockets and plugged vegetation are usually observed suggesting significant bio-karstic weathering (Giaccio et al., 2012, Bubeck et al. 2015). Typically, this section is not sampled for cosmogenic dating purpose (see Fig. 4) because the erosion might significantly affect the [^{36}Cl] signal. There are no data associated with this portion to constrain the exhumation of this upper and older portion, which however needs to be considered in the modelling since a significant amount of ^{36}Cl is accumulated at depth. We thus also account for that amount in the model as summarized in Fig. 4.

The total amount of ^{36}Cl accumulated in the sampled profile thus integrates : 1) the long-term inherited contribution (left panel in the Fig. 4), and 2) the ^{36}Cl accumulated during the seismic exhumation that includes the ^{36}Cl accumulated during the post-glacial exhumation of the uppermost fault plane, usually not sampled, called in the following the “post-glacial inheritance” (central panel in the Fig. 4), and the ^{36}Cl accumulated during the post-glacial exhumation on the sampled portion, called in the following “post-glacial exhumation” (right panel in the Fig. 4).

3. Modeling 36Cl profile and recovering exhumation histories

(i) Bayesian inference

Inferring the exhumational history of a post-glacial fault-plane from its in-situ ^{36}Cl content, means resolving the most probable number of events that progressively exhumed the fault-plane, their displacements and their ages. The use of Bayesian inferences is particularly well suited to this problem since it allows constructing a statistical model fitting the data, integrating *a priori* information on the parameters, and summarizing the results of each parameters by a probability distribution. Bayesian approaches have been successfully applied in cosmogenic geochronology (Muzikar and Granger, 2006; Schimmelpfennig et al., 2011; Marrero et al., 2016; Laloy et al. 2017) to date morphological surfaces, and in paleoseismology (e.g. Buck and Bard, 2007; Hilley and Young, 2008) to reconcile radiocarbon ages.

Here, we perform a “transdimensional” inversion (Sambridge et al. 2012) with the **reversible jump Markov chains Monte-Carlo** algorithm (RJ-MCMC, Green 1995) that allows a variable number of parameters.

A Bayesian inference aims at quantifying the *a posteriori* probability distribution of the model parameters, *m*, given the observed data, d_{obs}, noted as $p(m \mid d_{obs})$. Following Baye's rule, the posterior distribution is deduced from the combination of the model structure $p(d_{obs}|m))$ and the prior $p(m)$:

$$posterior \propto likelihood \times prior \quad (8)$$

$$p(m \mid d_{obs}) \propto p(d_{obs}|m)p(m) \quad (9)$$

where the likelihood function $p(d_{obs}|m)$, is the probability that the model reproduces the observed data given the model *m*. The prior $p(m)$ is the probability of the set of parameters *m*, representing our knowledge of *m* before performing the inference.

The posterior distribution thus represents how our prior knowledge of parameters *m* is able to reproduce data.

Posterior distributions are constructed by sampling the parameter space in such a way that the sampling density of each parameter reflects that of the posterior distribution. In order to infer the model parameters and its dimensionality, we have used the reversible-jump Markov chain Monte Carlo (rj-McMC) sampler based on the well-known Metropolis-Hasting algorithm (Metropolis et al., 1953; Hastings, 1970). The rj-McMC sampler is fully described in previous studies (Malinverno, 2002; Gallagher et al., 2011; Bodin et al. 2012), and the mathematical formulation can be found in the appendix of Bodin et al. (2012). A brief overview of the algorithm is proposed here.

The rj-McMC method iteratively performs a random walk in the parameter space, where the choice of each new model (set of parameters) of the walk only depends on the current model of the walk. The models of the chain are thus independent from each other. At each step, a new model is proposed from a random perturbation of the current model according to a proposal function (normal distribution with a fixed mean and standard deviation). The model is either accepted or rejected following an acceptance criterion (see Bodin et al. (2012) for more details). If the model is accepted, the new position represents one iteration, and the whole process is repeated. If the model is rejected, the walker remains in the same position, representing also one iteration. After an initial period ("burn-in" period) during which the random

walker progressively moves toward low misfit region(s), the chain is assumed to be stationary, meaning the parameter space tends to be sampled according to the **posterior probability distribution**. After a sufficient number of iterations, the ensemble of models (excluding the burn-in period) might thus provide a good approximation of the posterior distribution for the model parameters.

(ii) Model parameterization

We have used the rj-McMC library provided by Gallagher et al. (2011) (available at http://www.iearth.org.au/codes/rj-MCMC/), designed for 1D spatial problems. In this problem, the whole history of the post-glacial scarp is search and described by a variable number, *k*, of event(s) that exhumed distinct portion(s) of the fault-plane. The dimension of the exhumed portion(s) of the scarp are searched, as well as their exhumation age(s).

The rj-McMC library made use of Voronoi nuclei to parameterized a spatial model. The exhumed fault-plane can be viewed as a succession of "layers", or "portion" of the scarp exhumed, for which the number, the amplitude and the age of exhumation is searched. Each exhumed portion *i* of the fault-plane is described by the height of its Voronoi nucleus c_i, and by its age of exhumation a_i (Fig. 5). Those parameters are the variables directly searched by the algorithm. From the location of the nucleus c_i, it is possible to obtain the location of the interface(s) between each exhumed portion. An interface is defined as being the equidistant between adjacent nuclei (Fig. 5). The amplitude of each exhumed portion (i.e. the slip of each event) is obtained by subtracting the lower interface height of the upper one. To simplify the analysis of the results, we will directly look at the slip of the events and at the location of the interfaces between each exhumed portion of the scarp.

The model parameters *m*, to be inverted are thus, the number of events that exhumed distinct fault-plane portion (*k*), the slip amplitude(s) (*s*), and the age(s) (*a*). The history of the scarp prior the post-glacial exhumation is also parameterized by the peri-glacial slip-rate, *sr* (as previously explicated in section I.2). Finally, the model to be inverted is $m = [k, s, a, sr]$.

(iii) Choosing a new model

At each iteration, a new model is proposed by the reversible jump algorithm from the perturbation of the current model. This perturbation is randomly chosen between 4 potential moves:

- randomly choose an event i and perturb its age a_i, respecting the current chronology of event ages ($a_{i-1} > a_i > a_{i+1}$).
- randomly choose an event i and perturb the vertical position of its Voronoï nuclei c_i , inducing a change in the slip amplitudes.
- perturb the peri-glacial slip-rate *sr*.
- create a new event, randomly inserted in the chronology of event.
- randomly choose an event, and suppress it.

The dynamic parametrization of such transdimensional approach will thus adapt to the information provided by the ^{36}Cl data, naturally favoring the least complex models (principle of parsimony), i.e models with many events are naturally discouraged (Malinverno, 2002).

(iv) The forward model

Testing a model *m* of scarp exhumation requires computing the ^{36}Cl concentration that would theoretically be observed along the fault-plane height using a forward model. We have modified the *Modelscarp* model previously proposed by Schlagenhauf et al. (2010) to include 1- the latest muon production calculation from Balco et al. (2017) that includes LSD scaling procedure by Lifton et al. (2014), (Method 1B in Balco, 2017) 2- the long-term inheritance (see section I.2). In Schlagenhauf et al. (2010), the muon production rate is calculated with a single exponential function with a constant attenuation length of 1500 g/cm2. This approach does not correctly approximate the muon flux and in particular the increase of the muon energy with depth resulting in an increase of the instantaneous attenuation length with depth (see details in Balco, 2017). In our case, where the production at depth in the ^{36}Cl contribution is non-negligible, incorporating the correct calculation is important. We use the code of Balco (2017), to compute the muon flux by integrating their surface spectra.

Figure 6 shows a comparison of two ^{36}Cl profiles resulting from the same seismic history but with the model as in Schlagenhauf et al. (2010), (blue curve) and with our

new code incorporating the muon integration spectra as in Balco (2017), (yellow curve). There is a discrepancy of around 1% between those two models. This suggests that in this case, the approximation made using a constant attenuation length of 1500 g/cm^2 is negligible.

(v) The likelihood function

The likelihood function $p(d_{obs}|m)$ provides the probability of a tested scenario using the common Gaussian-based expression:

$$p(d_{obs}|m) = \frac{1}{\sqrt{(2\pi)^n}} \times exp\left\{\frac{\phi(m)}{2}\right\} \quad (10)$$

with *n*, the number of measurements, and $\phi(m)$, the misfit function. The weighted root mean square (RMSw) is used as a misfit function. It quantifies the fit between the measured and the modelled ^{36}Cl concentrations, taking into account the uncertainties on the measurements:

$$\phi(m) = \sqrt{\sum_{i=1}^{n}\left[\left(\frac{d_i - g(m)_i}{E_i}\right)^2\right] \Big/ n} \quad (11)$$

for each sample *i*, d_i is the measured [^{36}Cl], $g(m)_i$ is the modeled [^{36}Cl] and E_i is the uncertainty on the AMS measured [^{36}Cl].

(vi) The Prior distribution

The prior probability $p(m)$ of the searched parameters is *a priori* knowledge we have on certain parameters. The prior distribution might be rigorously chosen since it controls the final results (the posterior probability distribution). In order to reduce the influence of the prior, we set a uniform distribution for each searched parameter with large bounds, instead of a Gaussian density function centered on a particular value. In doing so, we allow the finals results to be dominated by the data, not by the prior**.** The prior distribution for the searched parameters are as presented below for all the tests presented in the following sections:

- the number of events that we set between 1 and 20 ($p(k) = \mathcal{U}(1,20)$, where $\mathcal{U}(a,b)$ is an uniform distribution with minimum and maximum values as *a* and *b*,
- an event age ranges between 0 and 20 ka ($p(a) = \mathcal{U}(0,20\ ka)$),

- an event slip ranges between 0 and the height of the scarp Hs ($p(s) = \mathcal{U}(0,Hs)$),
- the peri-glacial slip-rate of the fault ranges between 0 and 5 mm/yr ($p(sr) = \mathcal{U}(0,5\ mm/yr)$).

(vii) The Posterior distribution

Following the Bayesian formulation, the posterior distribution of all searched parameters is then written:

$$p(m \mid d_{obs}) \propto p(d_{obs} \mid k,a,s,sr)\, p(k)p(a)p(s)p(sr) \quad (12)$$

II. Inversion of synthetic datasets

To assess the ability of the algorithm, we conduct tests using synthetic [^{36}Cl] profiles as input data for the inversions. For each scenario case, we run 16 independent rj-McMC chains during 400 hours (maximum available computing time on our cluster), resulting in 100-150 x10^3 iterations. The first part of each chain (10-20 x10^3 models) is discarded because it corresponds to the burn-in period during which the chain converges toward the low misfit area.

(i) Characteristic earthquake scenario

The synthetic ^{36}Cl data results from: 1) a 300 kyr-long inheritance history with a fault slip-rate of 1 mm/yr prior the post-glacial exhumation, 2) a post-glacial inheritance corresponding to 4 events exhuming the upper not sampled fault-plane (slip of 2 m each, at 12, 14, 16 and 18 ka), and finally 3) the exhumation of 8 m of the fault-plane by 4 events of 2 m slip each at 1, 4, 7 and 10 ka. The site parameters are detailed in the Table A.1. For the chemical composition (majors and traces elements) we took the data from Schlagenhauf et al. (2010), (all data files are available with the code). The synthetic [^{36}Cl] profile is composed of one sample every 10 cm, with additional samples located below the colluvial wedge surface reaching a maximum depth of 2 m. Analytical uncertainties on samples are set at 4 x10^3 atoms of [^{36}Cl] per gram of rock, which corresponds to about 2-5 % uncertainty similarly to what is usually obtained on ^{36}Cl concentration. The ability of the algorithm to converge toward a reliable solution is assessed on Fig. 7. The evolution of the misfit over the iteration (Fig. 7-A) shows a

large decrease over the first 5000 models and then fluctuates between 20 and 2, with the most frequent misfit around 10 (Fig. 7-B), as expected for a Markov chain. The number of events also varies over the iterations (Fig. 7-C), starting at 1 and quickly increasing to 5-11 events, 6 events being the most frequent value (Fig. 7-D). The number of events is very rarely smaller than 5, suggesting that the [^{36}Cl] profile cannot be well resolved with less than 5 events. Plotting the age of the events over the iteration (Fig B.1 in Appendix B) shows that the algorithm well identified 4 events around 1.2 ka, 4.2 ka, 7.2 ka and 10.5 ka, on the sampled-part of the fault-plane. The algorithm yields one or two events for the upper not-sampled part of the fault-plane, the age of those events being much more variable, and assessed in most models around 16-20 ka.

Models having a larger number of events (> 6 events) generally shows the same pattern of ages, additional events being generally very close in age to the another one. Thus, those models reproduce the data as well than the 5-events-models but because the algorithm favors simpler models their occurrence is less frequent.

Similarly, when looking over the iterations at the interface locations between successive events along the fault-plane (Fig B.2 in Appendix B), it appears that 3 interfaces are well determined and stable around 2, 4 and 6 m high. Those correspond to the 4 well-identified event ages that exhumed the sampled-part of the fault-plane. The upper not-sampled part is less well constrained since we observe only one interface with a very variable position.

Figure 8-A shows the cumulative slip over time for the 740 000 models obtained from the 16 rj-McMC chains (burn-in period has been discarded), visualized through a density map. We represent the distribution of event ages in peaks of age occurrences, (Fig. 8-B). The distribution appears multimodal, with 4 Gaussians peaked at 1.1, 4.1, 7.1 and 10.5 ka. We delimit the highest density region (HDR) with red curves on the density map as corresponding to the 95% confidence interval (95% of the most frequent models) (Fig. 8-A). This interval allows defining the 2σ uncertainties on each event age and slip (see an example in Appx B.3). The resulting ages for the four events are E1 at 1.1 (-0.6/+0.8) ka, E2 at 4.1 (-0.6/+0.9) ka, E3 at 7.1 (-0.9/1.0) ka and E4 at 10.5(-1.0/0.9) ka, in very good agreement with the true values (e.g. 1, 4, 7, and 10 ka, see Table 1).

The slip of those events is determined using the distribution of the event interface locations along the fault-plane on Fig. 8-C. The distribution is also multi-modal with 3

well expressed Gaussian centered on 2, 4 and 6 m, and a small peak around 9.8 m, giving a slip of 2, 2, 2 and 3.9 m, respectively for E1, E2, E3 and E4. Similarly, we determine the 2σ uncertainties on the slip using the 95% HDR region (see an example in Appx B.3). We obtain 2.0 m (-0.4/+0.4) for E1, 2.0 m (-0.9/+0.8) for E2, 2.0 m (-0.8/+0.8) for E3, and 3.9 m (-2.9/+0.7) for E4, in very good agreement with the true values for the three youngest events and within uncertainty for E4 but clearly overestimated (e.g. 2 m each, see Table 1). Figure 9 shows the [^{36}Cl] profiles from the true scenario and the 100 best ones resulting from the algorithm, the comparison shows that the fit is excellent and slightly differs at 6 m high at the interface with the oldest event.

Concerning the not-sampled part of the fault-plane (above 8 m high), the models are more dispersed with a larger 95% HDR (Fig. 8-A) and no evident peak in the event ages and slip distribution, suggesting that various combination of event ages and slips are able to reproduce the dataset. Most of the models suggest this part of the scarp has been exhumed by only 1 or 2 events, while the synthetic scenario requires 4 events, the algorithm thus tends to under-estimate the number of events. The 95% HDR suggests that this part of the scarp has been exhumed between 20 ka and 9 ka, the scarp-top being 18-20 kyr old. Those values are in agreement with the synthetic scenario (Fig. 8-A) and yield a slip-rate of 1.0-1.1 mm/yr for the period 9-20 ka, similar to the one of the true scenario (1 mm/yr).

Fig. 8-D shows the distribution of the peri-glacial slip-rate obtained from the inversion. The distribution is widely dispersed between 0.2 and 5 mm/yr with the most frequent value at 1 mm/yr, corresponding to the value of the true scenario.

(ii) Clustered earthquakes scenario

We test here the ability of the algorithm to infer a scenario composed of clustered events in time. The scenario is composed of a first cluster of 4 events at 15.0, 15.5, 16.0 and 16.5 ka, that exhumed the upper not-sampled part of the fault-plane, and a recent cluster of events at 1.0, 1.5, 2.0 and 2.5 ka that exhumed the lowest sampled fault-plane. The displacement of each event is set at 2 m. The peri-glacial slip-rate is set at 1 mm/yr.

Figure 10 presents the results of the inversion based on the analysis of 140 000 models obtained from 16 independent chains. Two periods of activity are identified by the inversion at 0.9-3.5 ka and 14.5-20 ka. In more detail, two peaks can be identified in

the distribution of event ages (Fig. 10-B) at 1.5 and 2.5 ka, with a small peak interface located around 4 m and a large one around 8 m (Fig. 10-C). The inversion thus yields two events of about 4 m at 1.5 and 2.5 ka (-0.7/+1.5), while the true scenario is composed of 4 events of 2 m each between 1.0 and 2.5 ka. In such case, the algorithm is thus not able to decipher 0.5 kyr-clustered events. The inferred slips are thus larger but the inferred cumulative slip and the timing of the cluster are correctly estimated.

For the not-sampled part of the scarp, the yielded exhumation is between 14.5 and 20 ka with no peaks in the age distribution, suggesting that various combinations of age and slip are plausible within this range of ages. The yielded scenario is in agreement with the true scenario with uncertainties of about 5 kyr (20-30%). Similarly, the peri-glacial slip-rate is not well constrained (Fig. 10-D), with a small peak at 1.2 mm/yr, and a very large range of value going from 0.4 to 5 mm/yr.

(iii) Effect of quiescence period prior the post-glacial exhumation

a. **Case of a 20 m high scarp**

We explore here the possibility that the fault has experienced a period of quiescence prior the post-glacial exhumation, i.e prior 20 000 ka. We expect that the contribution from the inherited [^{36}Cl] would significantly increase in such case because the fault-plane has remained in the same position for a time longer than the recent exposure. We have tested this hypothesis by adding a quiescence period to the previous synthetic scenario. The scenario is composed of a recent cluster of 4 events at 1.0, 1.5, 2.0 and 2.5 ka (2 m of slip each) that exhumed the lower sampled fault-plane, and an older cluster of 4 events at 15.0, 15.5, 16.0 and 16.5 ka, that exhumed the upper not-sampled part of the fault-plane. Between 16.5 ka and 30 ka, the fault experienced a period of quiescence, during which the fault has not moved. Prior to 30 ka, the peri-glacial slip-rate is set at 1 mm/yr, simulating an older period of activity. For the inversion, the priors are thus similar to the previous presented scenarii and reminded here: 1) the number of events ranges between 1 and 20, the peri-glacial slip-rate ranges between 0 and 5 mm/yr, the age of the events ranges between 0 and 20 ka, and the slip ranges between 0 and 18 m (height of the scarp).

The results from the inversion of the synthetic [^{36}Cl] profile are in Figure 11. The inversion gave nearly the same results as the one obtained without including a quiescence period to the true scenario. The results differ for the estimation of the peri-

glacial slip-rate, which is peaked at 0.6 mm/yr, ranging from 0.4 to 2.2 mm/yr, thus smaller than in previously estimated clustered earthquake scenario.

b. Case of a small scarp sampled to the top

Here, we test a scenario with a smaller scarp, sampled near the top (such as MA2 and MA4 sites in Schlagenhauf et al. 2011). The true scenario corresponds to an 8-m-high post-glacial fault-scarp, sampled up to the top, exhumed by a cluster of 4 events at 5.0, 5.5, 6.0 and 6.5 ka, with 2 m of displacement each. This cluster has been preceded by a quiescence period that started at 30 ka, hence from 30 ka and 6.5 ka the fault has not moved. Before 30 ka, the peri-glacial slip-rate is set at 1 mm/yr, simulating an older period of activity. The priors for this inversion are thus: 1) the number of events ranges between 1 and 20, the peri-glacial slip-rate ranges between 0 and 5 mm/yr, the age of the events ranges between 0 and 20 ka, and the slip ranges between 0 and 8 m (height of the scarp).

The results of this inversion are presented in Appx B-4. We observe that the main period of activity is found between 2.0 and 3.5 ka, thus 1.5 ka younger than the timing of the cluster for the true scenario. A recent event is found between 0 and 2.5 ka with a slip of about 1 m, that does not match with an event of the true scenario. An additional event is observed at 19.9 ka with a very small slip (< 5 cm). The slip-rate is also very low and peaked at 0.2 mm/yr. Considering the difference between the results and true scenario, the inversion did not succeed in finding a model that well reproduce the data. The modeled [^{36}Cl] profile of the best model (in Fig. B-5) does not fit the synthetic [^{36}Cl] profile, especially at the base of the fault-plane, and below the colluvial wedge.

c. Recovering a quiescence period prior the exhumation of the fault-scarp

An additional test is proposed here using the same synthetic scenario, but including a quiescence period *Qs* as an additional parameter of the inversion. The quiescence is parameterized in the model by a period during which the fault remains in the same position before the oldest event. For this inversion, the priors on the parameters are thus: 1) the number of events (k) ranges between 1 and 20, the peri-glacial slip-rate (sr) ranges between 0 and 5 mm/yr, the age of the events (a) ranges between 0 and 20 ka, and the slip (s) ranges between 0 and 8 m (height of the scarp), and a quiescence

period (Qs) ranging between 0 and 50 kyr ($p(Qs) = \mathcal{U}(0{,}50\ kyr)$). In this case, the model to be inverted is thus *m = [k, s, a, sr, Qs]*.

The 95% HDR on the plot of the cumulative slip over the time obtained from the inversion (Fig. 12-A and B) suggests a cluster of events between 4.5 and 7.0 ka with a total displacement of 8 m, in agreement with the true scenario (4 events between 5 ka and 6.5 ka). Before this cluster of events, the algorithm found a period of quiescence that started around 30.5 ka (± 2 ka), also in agreement with the true scenario. The distribution of the peri-glacial slip-rate before the quiescence period is peaked at 1 mm/yr (-0.5/+2.5), suggesting the algorithm might be able, in this context, to infer a period of activity of the fault before a long quiescence period. The modeled [^{36}Cl] profile of the best model (in Appx B-6) also fit well with the synthetic [^{36}Cl] profile.

(iv) Slow slipping normal fault

We present a final test here that considers the case of a slow-slipping normal fault, i.e the fault has not moved during peri-glacial times, and the erosional processes mainly control the low dipping peri-glacial abrasion surface (see also section 2.2). The site is characterized by: 1) a colluvial wedge surface angle α=20°, 2) a fault-plane angle β=50°, and 3) an upper surface angle γ=30°. The peri-glacial inheritance is directly controlled by the denudation rate ε that progressively lowers the surface of the whole scarp (here ε=30 m/Myr). Note that the denudation-rate ε is taken as the vertical component of the upper surface lowering. Hence the rate of the samples along the fault-plane (*sr*) is obtained by the relation $sr = \varepsilon/\sin(\beta)$. The post-glacial exhumation of the 8 m high scarp is produced by 4 events at 5.0, 5.5, 15.0 and 15.5 ka (2 m of slip each). The post-glacial fault-scarp is sampled up to the top. The priors for this inversion are: 1) the number of events ranges between 1 and 20, 2) the age of the events ranges between 0 and 20 ka, and 3) the slip ranges between 0 and 8 m (height of the scarp), 4) the denudation-rate ranges between 0 and 500 m/Myr.

The 95% HDR on the plot of the cumulative slip over the time obtained from the inversion (Fig. 13-A and B) suggests two clusters of events around 5.4 and 15.4 ka with 4 m of displacement each, in agreement with the true scenario. Before this cluster

of events, the algorithm found a peri-glacial denudation of 30-40 m/Myr, also in agreement with the true scenario. This suggests the algorithm is able to account for the long-term inheritance produced by a long-term lowering surface. The modeled [^{36}Cl] profile of the best model (in Appx B-7) also perfectly fit with the synthetic [^{36}Cl] profile (Rmsw = 2.9).

III. Discussion

We have tested the ability of the algorithm to recover the exhumation history of a fault-plane in various settings, varying the histories (characteristic earthquakes, clustered earthquakes), varying the size of the scarp and the length of the sampling, and including a potential quiescence period during the peri-glacial period. Our results indicate that the use of a sampling algorithm is crucial to accurately infer exhumation histories from the modeling of [^{36}Cl] data. The results show that several models are able to fit the data within their analytical uncertainty, but most yielded *scenarii* enhance similar periods of exhumation. Those results thus reveal that despite the handful models that best explains the data, all yields a similar seismic history.

In the case of characteristic earthquakes, the inversion procedure has the ability to accurately recover the true scenario that exhumed the sampled fault-plane with a mean discrepancy relatively to the true model of 0.2 kyr (< 20 %) on the events ages, and 0.5 m (~15 %) on the displacements. The 2σ uncertainties on the ages are ~ 0.5 kyr, and those on the slips are ~0.5 m. The inferred scenario for the earliest fault history is less well constrained since the algorithm tends to significantly under-estimate the true number of events. However, the yielded scenario gives ages bracketing the ones of the true scenario, within 2σ uncertainties. Uncertainties on the ages are thus significantly larger than the ones yielded for the sampled portion of the fault-plane. The inversion is however very efficient in yielding the true slip-rate since the discrepancy between the model and the true scenario is of less than 0.1 mm/yr, thus yielding of less than 10%. This suggests that the algorithm is able to constrain the exhumation history of the not-sampled fault-plane, by the modeling of the inheritance. The yielded long-term fault slip-rate is also in very good agreement with the true one, but with a large spectrum of possible results (-0.5/+4 mm/yr). In that configuration, this suggests the impact of the peri-glacial slip-rate on the

final [^{36}Cl] profile appears relatively minor, probably because most ^{36}Cl is accumulated during the post-glacial period and thus the ^{36}Cl contribution during the long-term history is negligible. This effect is probably magnified by the fact that the sampled portion of the scarp only covers half of the scarp (10 m).

We have tested the algorithm with an exhumation scenario that includes clustered earthquakes. The results of the inversion suggest the algorithm is clearly able to detect an acceleration in the fault slip history. While individual events cannot be resolved during the cluster in that scenario, the algorithm is able to accurately provide the timing of the acceleration with a 2σ uncertainty of 1-2 kyr. The total amount of displacement during a cluster is also well estimated with a discrepancy < 10 cm, and an uncertainty of -0.2/+0.5 m. It is likely that individual events cannot be deciphered because there are too close in time, producing an insignificant variation in the [^{36}Cl] profile. For the not-sampled part of the fault-plane, the algorithm yield a large range of ages with a subtle peak around 15.5 kyr, close to the age of the earlier cluster of the true scenario. So, although the number of recovered events is not well constrained for this portion of the scarp, and generally under-estimated, the algorithm is still able to accurately recover a period of fault slip acceleration during this period. Finally, the long-term slip-rate is not well constrained with a wide range of values. All in all, we observe that, in the case of clustered earthquakes, the algorithm is not able to decipher individual events, but instead it accurately identifies the period(s) of acceleration and quiescence of the fault, in others words the slip variability over the post-glacial period.

We have tested the impact of the peri-glacial history on the final inferred scenario, and in particular the occurrence of a quiescence period prior to the post-glacial exhumation (i.e. prior 18-21 ka). The first test made on a 16 m high scarp, sampled up to 8 m high shows that the algorithm is able to accurately account for the period of acceleration of the fault during the post-glacial period suggesting that the impact of a quiescence period prior the post-glacial exhumation on the inferred scenario is almost insignificant. The second test made on a 8 m high scarp, sampled up to the top, with a long quiescence period prior the post-glacial exhumation yield a 1-2 kyr shift (~40%) in the age of the slip acceleration. We also observe a typical behavior of the algorithm that found an event close to the upper age bound, with a negligible displacement. This suggests that the algorithm naturally tried to add a quiescence period, but is blocked by the upper age boundary. Moreover, the

inferred [^{36}Cl] does not fit the synthetic profile at depth which also strongly suggests that the inherited [^{36}Cl] is not correctly estimated. Even if the peri-glacial slip-rate is found very low (0.2 mm/yr) which allows to "artificially" increase the amount of inherited ^{36}Cl, it is still not enough to reproduce a 30 kyr long quiescence period. In such setting with a small scarp, the occurrence of a quiescence period thus significantly impact the inferred results, and the algorithm is not able to provide reliable results. To overcome this problem, it is necessary to add a quiescence period as an additional parameter of the inversion, to be able to fully reproduce the data.

The results obtained when adding a quiescence period shows the great ability of the algorithm to recover the true scenario with a discrepancy on the age of the cluster < 0.5 kyr and a 2σ uncertainty < 1 kyr. The discrepancy on the inferred quiescence period relatively to the true scenario is about 0.5 kyr, with an uncertainty of ± 1 kyr. The peri-glacial slip-rate inferred prior the quiescence period is also well estimated with a discrepancy of less than 0.1 mm/yr and an uncertainty of -0.5/+2.5 mm/yr. Thus adding a quiescence period allows to closely fit the synthetic [^{36}Cl] profile, especially at depth because the inherited ^{36}Cl is correctly estimated.

In the case of a slow slipping fault, the inherited [^{36}Cl] is mainly controlled by the rate at which the surface has been denudated and lowered. The results of the inversion show that the algorithm is clearly able to infer the true scenario of exhumation, detecting the two periods of acceleration, with a 2σ uncertainty of 1 kyr. The total amount of displacement during a cluster is also well estimated with a discrepancy < 10 cm, and an uncertainty of -0.4/+0.2 m. The peri-glacial denudation rate is also very well constrained with an uncertainty of ± 5 m/Myr, suggesting that the inherited [^{36}Cl] produced by the denudation of the upper surface has a major impact on the final [^{36}Cl] profile.

All in all, our results demonstrate the ability of the transdimensional approach to constrain the exhumation history of a fault-plane from the ^{36}Cl data, providing reliable information on the timing and the magnitude of the exhumational events. We have shown that the parsimonious approach, favoring less-complex models given the dataset, allows to avoid over-parameterized scenarios. Our procedure also allows precisely determining the uncertainties on the exhumation scenario. Concerning the exhumation scenario of the sampled part of the fault-plane, the discrepancy on the age of the events are generally < 0.5 kyr, and < 0.5 m on the slip.

The ^{36}Cl budget is divided into the proportion produced during the inheritance, at depth, which is modeled through the inherited part of the model and the proportion produced once the scarp is exhumed through seismic events. Thus if this proportion varies, so will the seismic event ages. On the other hand, the slip of event is not significantly affected by the inheritance, because it mainly depends on the location of the main discontinuities in the [^{36}Cl] profile, which are in general preserved independently of the inheritance. The inversion procedure allows "deconvoluting" the inherited [^{36}Cl] contribution and the ^{36}Cl produced by the post-glacial seismic exhumation, because those two phases produce different [^{36}Cl] profile shape. While, the first phase produces a large exponential decrease at depth, mostly controlled by the attenuation length of the muons, the latter produces cups and discontinuities in the [^{36}Cl] profile because the production is mainly neutron dominated, which usually affects the first 2 m of a previously buried fault plane (Schlagenhauf et al. 2010, as shown by Fig. 4). Various authors such as Stone et al. (1998) or Braucher et al. (2009) have shown that theoretically 2 concentrations values along a depth profile are sufficient to constrain the surface exposure age and rate of denudation. In our case, the large number of samples thus theoretically enables to decipher the various ^{36}Cl build-up contributions.

The samples taken from the fault-plane surface integrate a significant amount of "inherited" ^{36}Cl (up to 35%), that has been accumulated: 1) during the post-glacial period, prior the exhumation of the sampled fault-plane, and 2) prior the post-glacial period, during peri-glacial times. The inheritance is favored by 1) the low colluvial wedge density (usually ~1.5 g.cm2) that less attenuates cosmic rays and thus promotes the ^{36}Cl production at greater depth, and 2) by the geometry of the scarp (e.g. the difference between the fault plane dipping angle (β) and the colluvium surface dipping angle (α) that controlled the thickness of the colluvial wedge above the fault plane and thus both the shielding of cosmic rays and the attenuation length through the colluvium.

The novelty of our inversion procedure is to constrain, at the same time, 1) the history of the whole fault-plane, and 2) the behavior of the fault during the peri-glacial periods through its slip-rate, and a potential quiescence period. In particular, we show that ignoring the peri-glacial history of the fault can lead to a discrepancy on the inferred event ages up to several thousand years. We observe that in such situation, the [^{36}Cl] profile of the data is generally not well reproduced by the models, especially at depth. This situation could also be revealed when an event is found by the inversion with an age close to the

743 upper search limit and with a negligible displacement. In Schlagenhauf et al. (2010) and
744 more recently in Beck et al. 2018, and Cowie et al. 2017, the ^{36}Cl modelling procedure
745 does not account for this longer-term history.

746 In Figure 14 we compare the [^{36}Cl] profile below the colluvial wedge when considering a
747 long-term inheritance prior to the post-glacial exhumation (300 kyr with a slip-rate of 0.5
748 mm/yr) with a [^{36}Cl] profile accounting for a fixed period of inheritance prior to the post-
749 glacial exhumation (7 kyr, as it was done in Schlagenhauf et al. 2010, term in the
750 modelling called “pre-exposure”). The comparison show that both the shape of the profile
751 and the final amount of ^{36}Cl are significantly different and that the previous published
752 models overestimated the ^{36}Cl contribution near the surface, and underestimated it at
753 greater depth (30% and 70% respectively in that example).

754 Overall, our results suggest that the exhumation history of the whole fault-scarp has to be
755 modelled to fairly estimates the inherited ^{36}Cl, and obtain an accurate history. An over
756 simplification of this history could potentially lead to misestimate the inherited ^{36}Cl
757 accumulated by up to 60-70 %, resulting in a shift of the age of the event.

758 Here we have considered the colluvial wedge as static and not aggraded during the post-
759 glacial period, while some authors have shown that it can be faulted and argues that it
760 could also have undergone erosion or sedimentation (Galli et al., 2012). Without absolute
761 dating and systematic study of the colluvial wedge, we are not able to provide quantitative
762 answer to that issue. However we note that sampling sites are usually situated away from
763 gullies that potentially carry sediments and/or erode the colluvial wedge. If the colluvial
764 wedge experienced sedimentation, we expect the displacement of the events to be
765 underestimated. If so, it is also possible that some small events are missed. In any case,
766 absolute dating coupled with geophysical investigation of the colluvial wedge are required
767 to constrain its dynamic and deal with this issue.

768 Our new procedure of inversion thus allows to better model the exhumation history of the
769 fault-plane, but also enables to obtain quantitative information about the displacement of
770 the fault prior the exhumation of the sampled fault-plane. Sampling the fault-plane below
771 the colluvial wedge brings considerable constrains on the inherited ^{36}Cl, thus reducing the
772 uncertainties on the exhumation scenario, and improving the quality of the information
773 inferred for the peri-glacial period.

A perspective of this improvement is the possibility to quantify the activity of normal faults that have not produced post-glacial fault-scarp. Many normal faults exhibit morphological features attesting for their long-term activity (perched valleys, triangular facets…) but without strong evidences of post-glacial activation. In such cases, sampling the fault-plane below the colluvial wedge would thus theoretically provide the way to estimate the slip-rate of the fault during the peri-glacial period.

As previously shown by Schlagenhauf et al. (2010), deciphering individual events from the ^{36}Cl data is not systematically possible, especially when events are very close in time, or when the displacement are too small. Our tests strengthen the idea that the inferred number of events is always a minimum. Sensibility tests could allow determining the condition (minimum inter-event time, minimum displacement) to distinguish events for a particular sampling site. However, we show here that the algorithm provides the ability to precisely constrain the evolution of the slip-rate over the time, and precisely identify the period of acceleration and the period of quiescence of the fault during the post-glacial periods.

IV. **Conclusions**

We develop a new methodology to inverse the ^{36}Cl data acquired on a fault plane and deduce its seismic history of exhumation. First we modified the Modelscarp model from Schlagenhauf et al. (2010) that enables to calculate theoretical [^{36}Cl] profiles, in order to integrate a new calculation of the inheritance that better accounts for the long-term exhumation of the samples. This new version of Modelscarp also include the muon production calculation from Balco (2017) and Lifton et al. (2014). The Bayesian inference of ^{36}Cl data is performed using the reversible jump Markov chains Monte-Carlo algorithm, in order to jointly determine the probability on the number of events that have exhumed the fault-scarp, their ages and the amplitude of the displacements. The Modelscarp Inversion code is a stand-alone program available in the present article. This inversion procedure is able to provide results in couple of days with a precision < 0.5 kyr on the event ages, and < 0.5 m on the displacements.

Our tests revealed that a spectra of scenarios are generally able to reproduce the ^{36}Cl, but

all are merging towards similar periods of activity slightly varying around the same age and slip per event. This procedure thus finally enables to precisely assess the range of plausible scenario both for the inheritance, and for the exhumation of the sampled fault-plane itself. We observed that the range of solution is usually quite focused, especially when the inheritance is well constrained by samples taken below the surface of the colluvial wedge. In our tests, the uncertainties range from 0.5 kyr to ~2 kyr for the event ages, and are around 0.5 m for the slip.

A major finding is the impact of the fault activity prior the post-glacial exhumation on the final amount of ^{36}Cl, in some cases representing up to 35%. Our test reveal that ignoring this contribution might result in a shift of event ages by 1-2 kyr. Our model allows to better account for the inherited ^{36}Cl, and provide for the first time the way to quantify the activity of the fault prior the post-glacial period, i.e. over the last 30-50 kyr, from the ^{36}Cl contained in the fault-plane.

Those two sources of uncertainties (inheritance and analytical uncertainties) limits the ability of the ^{36}Cl profile approach to identify individual earthquakes on the fault plane except for earthquakes producing large displacement and/or separated by a significant inter-seismic period. Instead, we show that the ^{36}Cl profile approach is able to clearly distinguish and date periods of fault activity and periods of quiescence or low slip activity. Our interpretation thus enable to derive a continuous record of the slip-rate over time, precisely estimating all uncertainties. The deduced slip-rate history could thus be directly used in probabilistic seismic hazard assessment and thus account for the time variability which clearly lacks up to now in most seismic hazard model (Visini and Pace, 2014).

V. Code availability

The source code for Modelscarp Inversion is avalaible in a Git repository hosted at: https://github.com/jimtesson/Modelscarp_Inversion. Documentation and installation instructions for the most current release version of Modelscarp Inversion are provided at https://github.com/jimtesson/Modelscarp_Inversion/README.pdf. As far as we know, Modelscarp Inversion will operate on any system that meets the software requirements described in the README file. To date, Modelscarp Inversion is known to work on, and is tested for Mac, Linux platforms. Modelscarp Inversion and its components are distributed under a GNU GPLv3 open-source license.

VI. **Acknowledgment**

We warmly thank D. Bourlès, R. Braucher, M. Rizza, V. Godard, J. Chéry and M. Ferry for fruitful discussions, and one anymous reviewer as well as the associated editor for their comments that greatly improve the manuscript. Inversions were operated at the OSU-PYTHEAS HPC facility. We kindly thank the staff of the OSU-PYTHEAS HPC facility for their useful help. This work was financially supported by Labex OT-Med (FEARS and RISKMED projects).

VII. **References**

Akçar, N., Tikhomirov, D., Ozkaymak, C., Ivy-Ochs, S., Alfimov, V., Sozbilir, H., Uzel, B., Schluchter, C., 2012. 36Cl exposure dating of paleoearthquakes in the Eastern Mediterranean: First results from the western Anatolian Extensional Province, Manisa fault zone, Turkey. Geol. Soc. Am. Bull. 124, 1724–1735.

Armijo, R., Lyon-Caen, H., Papanastassiou, D., 1992. East-west extension and Holocene normal-fault scarps in the Hellenic arc. Geology 20, 491–494.

Balco, G., 2017. Production rate calculations for cosmic-ray-muon-produced 10 Be and 26 Al benchmarked against geological calibration data. Quat. Geochronol. 39, 150–173. https://doi.org/10.1016/j.quageo.2017.02.00

Benedetti, L., Finkel, R., King, G., Armijo, R., Papanastassiou, D., Ryerson, F.J., Flerit, F., Farber, D., Stavrakakis, G., 2003. Motion on the Kaparelli fault (Greece) prior to the 1981 earthquake sequence determined from 36Cl cosmogenic dating. Terra Nova 15, 118–124. https://doi.org/10.1046/j.1365-3121.2003.00474.x

Benedetti, L., Finkel, R., Papanastassiou, D., King, G., Armijo, R., Ryerson, F., Farber, D., Flerit, F., 2002. Post-glacial slip history of the Sparta fault (Greece) determined by ^{36} Cl cosmogenic dating: Evidence for non-periodic earthquakes. Geophys. Res. Lett. 29, 87-1-87–4. https://doi.org/10.1029/2001GL014510

Benedetti, L., Manighetti, I., Gaudemer, Y., Finkel, R., Malavieille, J., Pou, K., Arnold, M., Aumaître, G., Bourlès, D., Keddadouche, K., 2013. Earthquake synchrony and clustering on Fucino faults (Central Italy) as revealed from in situ ^{36} Cl exposure dating. J. Geophys. Res. Solid Earth 118, 4948–4974. https://doi.org/10.1002/jgrb.50299

Braucher, R., Del Castillo, P., Siame, L., Hidy, A.J., Bourlés, D.L., 2009. Determination of both exposure time and denudation rate from an in situ-produced 10Be depth profile: A mathematical proof of uniqueness. Model sensitivity and applications to natural cases. Quat. Geochronol. 4, 56–67. https://doi.org/10.1016/j.quageo.2008.06.001

Braucher, R., Merchel, S., Borgomano, J., Bourlès, D.L., 2011. Production of cosmogenic radionuclides at great depth: A multi element approach. Earth Planet. Sci. Lett. 309, 1–9. https://doi.org/10.1016/j.epsl.2011.06.036

Bubeck, A., Wilkinson, M., Roberts, G.P., Cowie, P.A., McCaffrey, K.J.W., Phillips, R., Sammonds, P., 2015. The tectonic geomorphology of bedrock scarps on active normal faults in the Italian Apennines mapped using combined ground penetrating radar and terrestrial laser scanning. Geomorphology 237, 38–51. https://doi.org/10.1016/j.geomorph.2014.03.011

Carcaillet, J., Manighetti, I., Chauvel, C., Schlagenhauf, A., Nicole, J.-M., 2008. Identifying past earthquakes on an active normal fault (Magnola, Italy) from the chemical analysis of its exhumed carbonate fault plane. Earth Planet. Sci. Lett. 271, 145–158. https://doi.org/10.1016/j.epsl.2008.03.059

Cowie, P.A., Phillips, R.J., Roberts, G.P., McCaffrey, K., Zijerveld, L.J.J., Gregory, L.C., Faure Walker, J., Wedmore, L.N.J., Dunai, T.J., Binnie, S.A., Freeman, S.P.H.T., Wilcken, K., Shanks, R.P., Huismans, R.S., Papanikolaou, I., Michetti, A.M., Wilkinson, M., 2017. Orogen-scale uplift in the central Italian Apennines

drives episodic behaviour of earthquake faults. Sci. Rep. 7, 44858. https://doi.org/10.1038/srep44858

Galli, P., Messina, P., Giaccio, B., Peronace, E., Quadrio, B., 2012. Early Pleistocene to Late Holocene activity of the Magnola fault (Fucino fault system, central Italy). Boll. Geofis. Teor. Ed Appl. 53, 435–458.

Giaccio, B., Galli, P., Messina, P., Peronace, E., Scardia, G., Sottili, G., Sposato, A., Chiarini, E., Jicha, B., Silvestri, S., 2012. Fault and basin depocentre migration over the last 2 Ma in the L'Aquila 2009 earthquake region, central Italian Apennines. Quat. Sci. Rev. 56, 69–88. https://doi.org/10.1016/j.quascirev.2012.08.016

Giaccio, B., Regattieri, E., Zanchetta, G., Wagner, B., Galli, P., Mannella, G., Niespolo, E., Peronace, E., Renne, P.R., Nomade, S., Cavinato, G.P., Messina, P., Sposato, A., Boschi, C., Florindo, F., Marra, F., Sadori, L., 2015. A key continental archive for the last 2 Ma of climatic history of the central Mediterranean region: A pilot drilling in the Fucino Basin, central Italy. Sci. Drill. 20, 13–19. https://doi.org/10.5194/sd-20-13-2015

Giraudi, C., Frezzotti, M., 1997. Late Pleistocene glacial events in the central Apennines, Italy. Quat. Res. 48, 280–290.

Giraudi, C., Frezzotti, M., 1995. Palaeoseismicity in the Gran Sasso Massif (Abruzzo, central Italy). Quat. Int. 25, 81–93.

Gosse, J.C., Phillips, F.M., 2001. Terrestrial in situ cosmogenic nuclides: theory and application. Quat. Sci. Rev. 20, 1475–1560.

He, H., Wei, Z., Densmore, A., 2016. Quantitative morphology of bedrock fault surfaces and identification of paleo-earthquakes. Tectonophysics. https://doi.org/10.1016/j.tecto.2016.09.032

Lifton, N., Sato, T., & Dunai, T. J. (2014). Scaling in situ cosmogenic nuclide production rates using analytical approximations to atmospheric cosmic-ray fluxes. *Earth and Planetary Science Letters*, *386*, 149-160.

Mitchell, S.G., Matmon, A., Bierman, P.R., Enzel, Y., Caffee, M., Rizzo, D., 2001. Displacement history of a limestone normal fault scarp, northern Israel, from cosmogenic ^{36}Cl. J. Geophys. Res. Solid Earth 106, 4247–4264. https://doi.org/10.1029/2000JB900373

Mouslopoulou, V., Moraetis, D., Benedetti, L., Guillou, V., Bellier, O., Hristopulos, D., 2014. Normal faulting in the forearc of the Hellenic subduction margin: Paleoearthquake history and kinematics of the Spili Fault, Crete, Greece. J. Struct. Geol. 66, 298–308. https://doi.org/10.1016/j.jsg.2014.05.017

Piccardi, L., Gaudemer, Y., Tapponnier, P., Boccaletti, M., 1999. Active oblique extension in the central Apennines (Italy): evidence from the Fucino region. Geophys. J. Int. 139, 499–530.
Sambridge, M., 1999. Geophysical inversion with a neighbourhood algorithm—II. Appraising the ensemble. Geophys. J. Int. 138, 727–746.

Schlagenhauf, A., 2009. Identification des forts séismes passés sur les failles normales actives de la région Lazio-Abruzzo (Italie centrale) par'datations cosmogéniques'(36Cl) de leurs escarpements. Grenoble 1.
Schlagenhauf, A., Gaudemer, Y., Benedetti, L., Manighetti, I., Palumbo, L., Schimmelpfennig, I., Finkel, R., Pou, K., 2010. Using in situ Chlorine-36 cosmonuclide to recover past earthquake histories on limestone normal fault scarps: a reappraisal of methodology and interpretations: Using 36Cl to recover past earthquakes. Geophys. J. Int. no-no. https://doi.org/10.1111/j.1365-246X.2010.04622.x

Schlagenhauf, A., Manighetti, I., Benedetti, L., Gaudemer, Y., Finkel, R., Malavieille, J., Pou, K., 2011. Earthquake supercycles in Central Italy, inferred from 36Cl exposure dating. Earth Planet. Sci. Lett. 307, 487–500. https://doi.org/10.1016/j.epsl.2011.05.022

Tesson, J., Pace, B., Benedetti, L., Visini, F., Delli Rocioli, M., Arnold, M., Aumaître, G., Bourlès, D.L., Keddadouche, K., 2016. Seismic slip history of the Pizzalto fault (central Apennines, Italy) using in situ-produced ^{36}Cl cosmic ray exposure dating and rare earth element concentrations. J. Geophys. Res. Solid Earth 121, 1983–2003. https://doi.org/10.1002/2015JB012565

Tucker, G.E., McCoy, S.W., Whittaker, A.C., Roberts, G.P., Lancaster, S.T., Phillips, R., 2011. Geomorphic significance of postglacial bedrock scarps on normal-fault footwalls. J. Geophys. Res. Earth Surf. 116, n/a-n/a.

https://doi.org/10.1029/2010JF001861

Visini, F., Pace, B., 2014. Insights on a Key Parameter of Earthquake Forecasting, the Coefficient of Variation of the Recurrence Time, Using a Simple Earthquake Simulator. Seismol. Res. Lett. 85, 703–713. https://doi.org/10.1785/0220130165

Wiatr, T., Papanikolaou, I., Fernández-Steeger, T., Reicherter, K., 2015. Bedrock fault scarp history: Insight from t-LiDAR backscatter behaviour and analysis of structure changes. Geomorphology 228, 421–431. https://doi.org/10.1016/j.geomorph.2014.09.021

Wilkinson, M., Roberts, G.P., McCaffrey, K., Cowie, P.A., Faure Walker, J.P., Papanikolaou, I., Phillips, R.J., Michetti, A.M., Vittori, E., Gregory, L., Wedmore, L., Watson, Z.K., 2015. Slip distributions on active normal faults measured from LiDAR and field mapping of geomorphic offsets: an example from L'Aquila, Italy, and implications for modelling seismic moment release. Geomorphology 237, 130–141. https://doi.org/10.1016/j.geomorph.2014.04.026

970

Appendix A

Table A.1: Parameters used for the modeling of [^{36}Cl] profiles.

Site-specific parameters
Geometric parameters: Hfinal = 18 m, $\alpha = 20°$, $\beta = 50°$, $\gamma = 30°$
Density: $\rho_{rock} = 2.7$ g.cm^{-3}, $\rho_{coll} = 1.5$ g.cm^{-3}
Scaling factors: fast neutrons = 2.750, muons = 1.703
Fault-plane erosion: $\varepsilon = 0.0$ mm /yr
Production rate parameters
Spallation on Ca: $\Psi^{36}Cl_{CaO} = 42.2 \pm 4.5$ at. of ^{36}Cl. g of Ca.yr^{-1} (Schimmelpfennig et al. 2011)
Spallation on K: $\Psi^{36}Cl_{K} = 162 \pm 24$ at. of ^{36}Cl. g of K.yr^{-1} (Evans et al. 1997)
Spallation on Ti: $\Psi^{36}Cl_{Ti} = 13 \pm 3$ at. of ^{36}Cl. g of Ti.yr^{-1} (Fink et al. 2000)
Spallation on Fe: $\Psi^{36}Cl_{Fe} = 1.9 \pm 0.2$ at. of ^{36}Cl. g of Fe.yr^{-1} (Stone et al. 2005)
Slow negative muons stopping rate at land surface: $\Psi\mu,0 = 190$ muon.g^{-1}.yr^{-1} (Heisinger et al. 2002)
Neutron attenuation length: $\Lambda f = 208$ g.cm^{-2} (Gosse and Phillips, 2001)
Neutron apparent attenuation length for a horizontal unshielded surface: $\Lambda f,h = 160$ g.cm^{-2}
Muon apparent attenuation length for a horizontal unshielded surface: $\Lambda\mu,h = 1500$ g.cm^{-2}

Appendix B

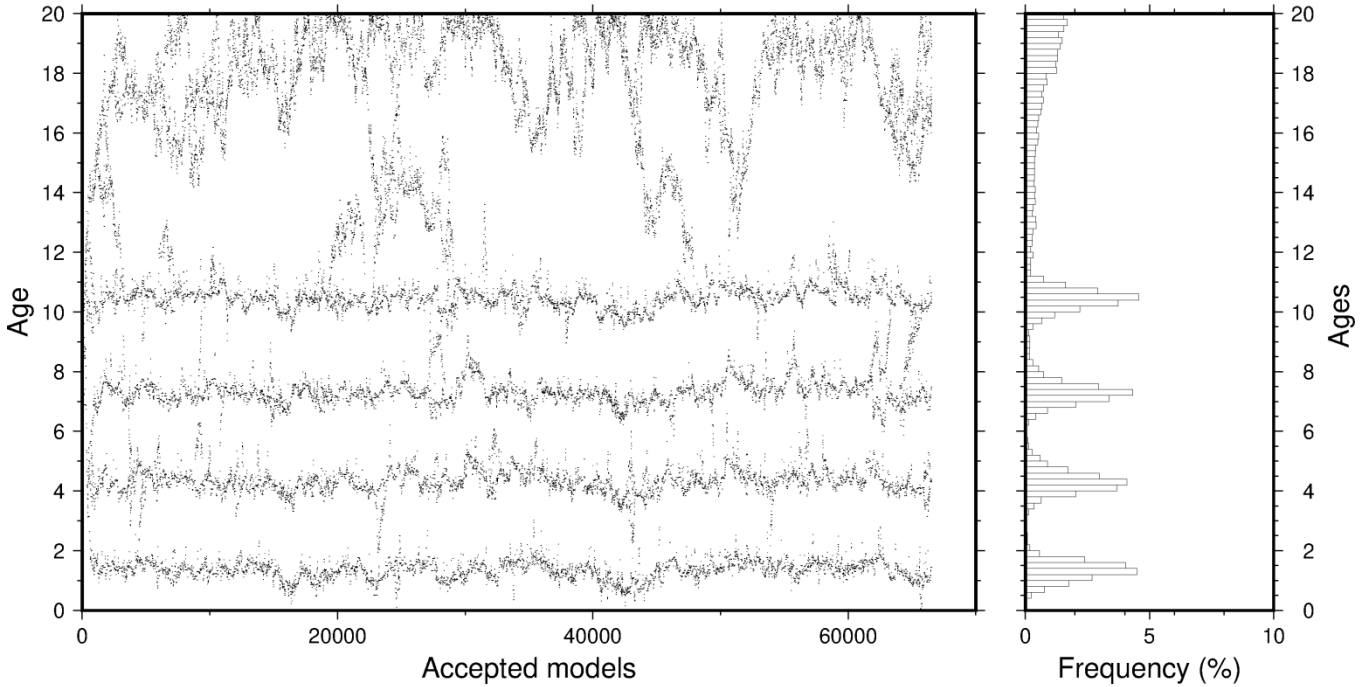

Figure B.1: Inversion of a synthetic [^{36}Cl] profile sampled up to 8m high on the fault-plane. Left panel: Evolution of the event ages over the iteration. Right panel: distribution of event ages when considering models after the burn' in period.

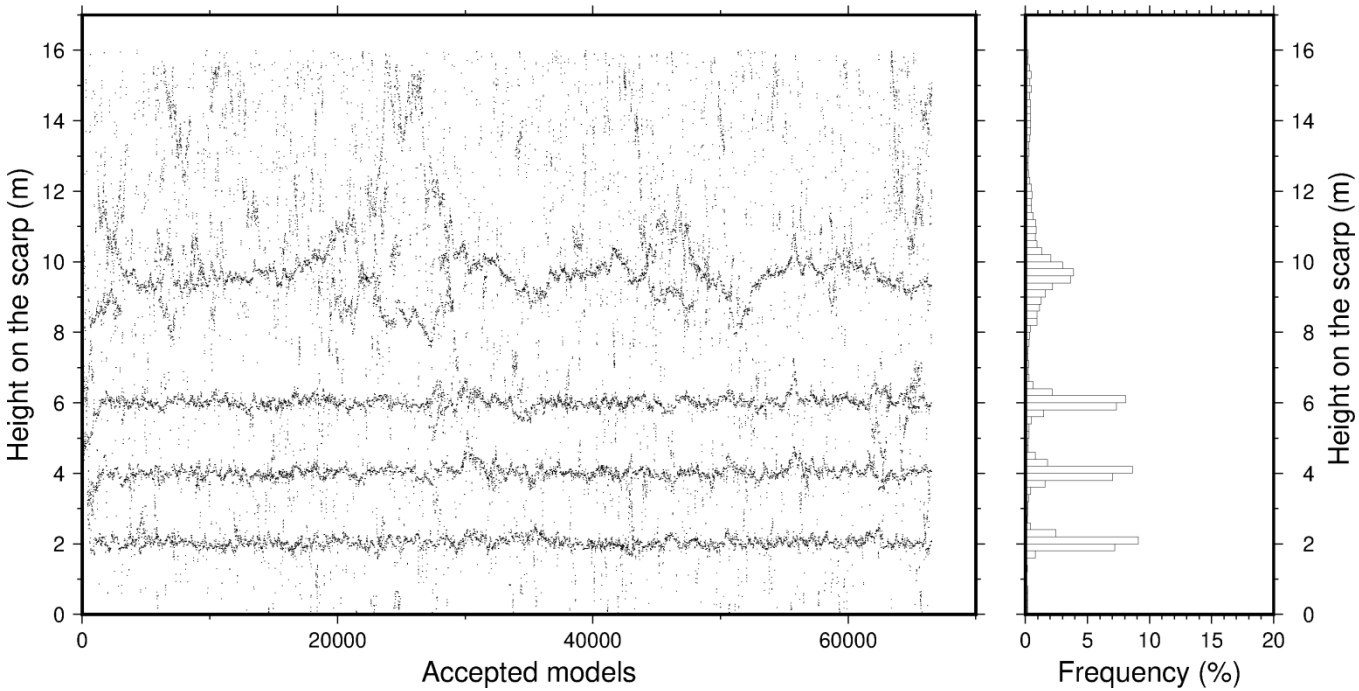

Figure B.2: Inversion of a synthetic [^{36}Cl] profile sampled up to 8m high on the fault-plane. Left panel: Evolution of the interface locations along the fault-plane over the iterations. Right panel: distribution of interface locations along the fault-plane when considering models after the burn' in period (10 000 iterations).

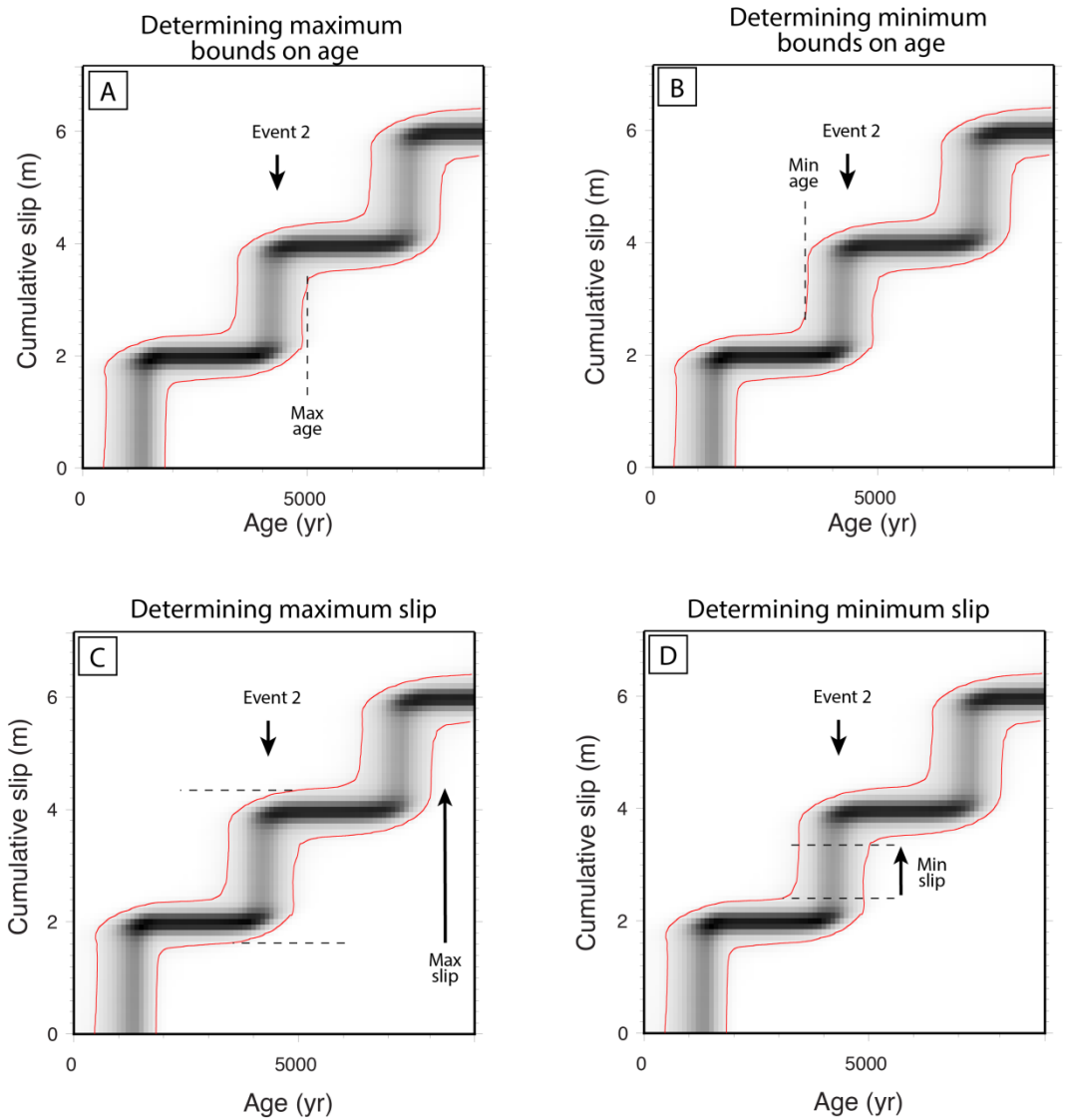

Figure B.3: Determining 2σ uncertainties on event ages and slips using the maximum and minimum bounds on the 95% HDR (highest density region). A) determining maximum bound on age, B) minimum bound on age, C) maximum bound on slip, D) minimum bound on slip.

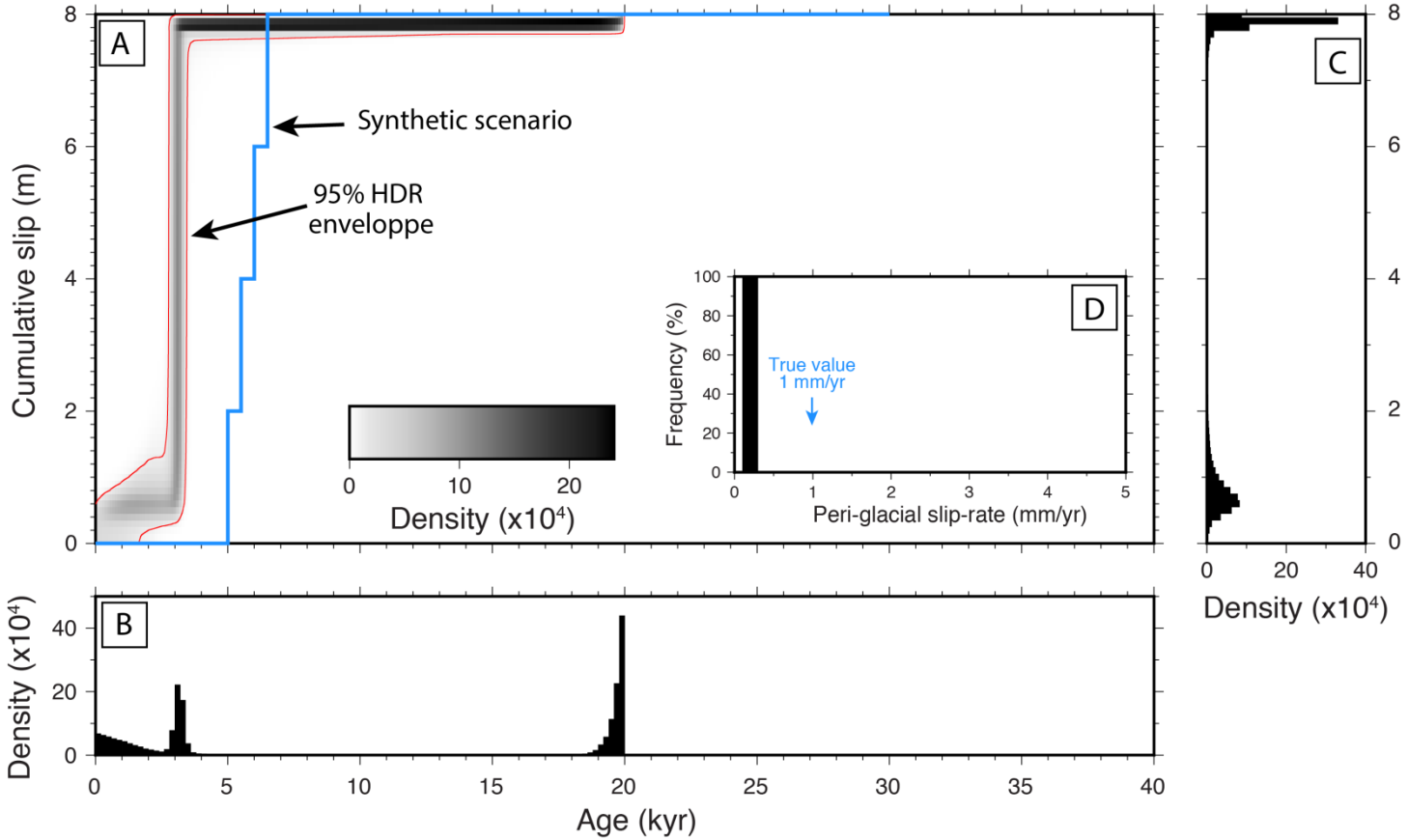

Figure B.4: Results inferred from the inversion of the synthetic [^{36}Cl] profile of a 8 m fault-plane. The synthetic scenario used for the inversion is composed of single cluster of 4 events at 1.0-2.5 ka, and a quiescence period between 30 and 2.5 ka. A) Density plot of the cumulative slip over the time obtain from models of the rj-McMC chain (about 110 000 models), compared with the synthetic scenario (blue). The highest density region (HDR), figured by the red envelop, includes the 95% most frequent models. B) Density distribution of event ages. C) Density distribution of the location of interfaces between the successive events along the fault-plane. D) Distribution of the peri-glacial slip-rate.

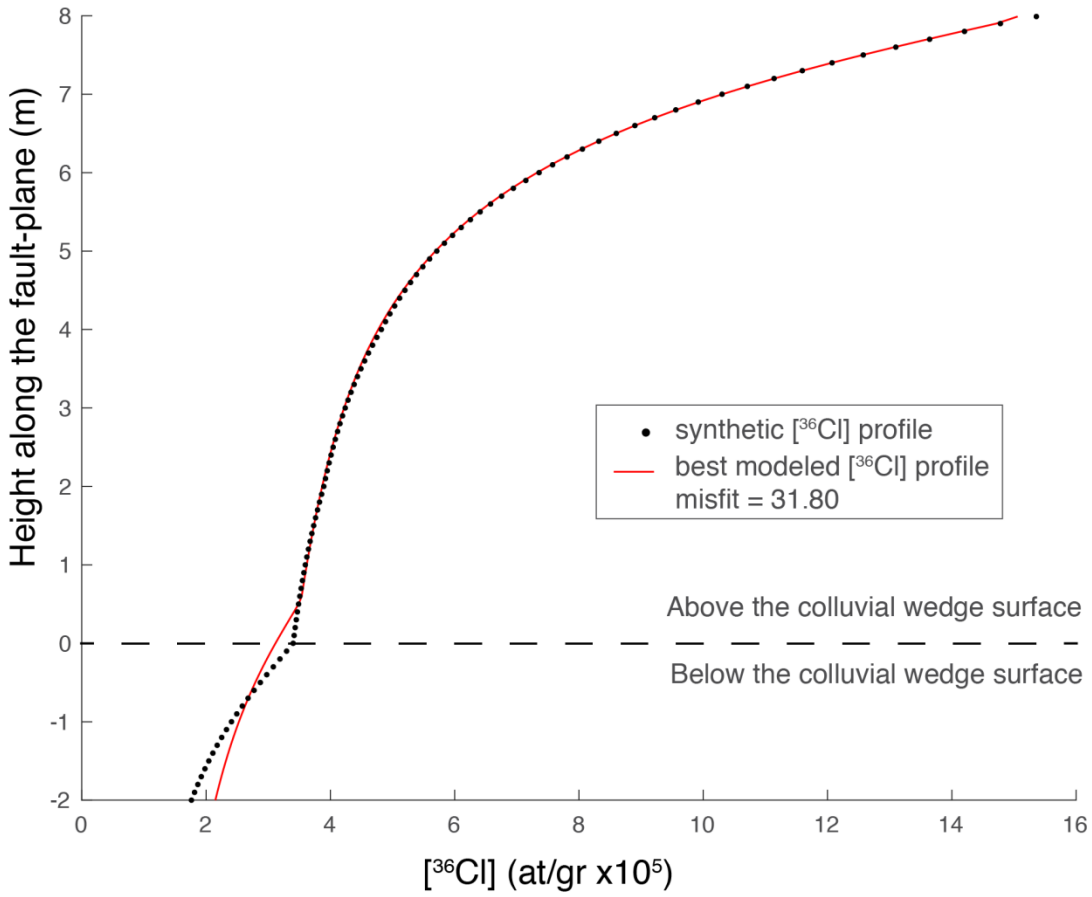

Figure B.5: Results inferred from the inversion of the synthetic [^{36}Cl] profile of a 8 m fault-plane. The synthetic scenario used for the inversion is composed of single cluster of 4 events at 1.0-2.5 ka, and a quiescence period between 30 and 2.5 ka. The synthetic [^{36}Cl] profile (black dots) is compared with the [^{36}Cl] profile of the best model (red line).

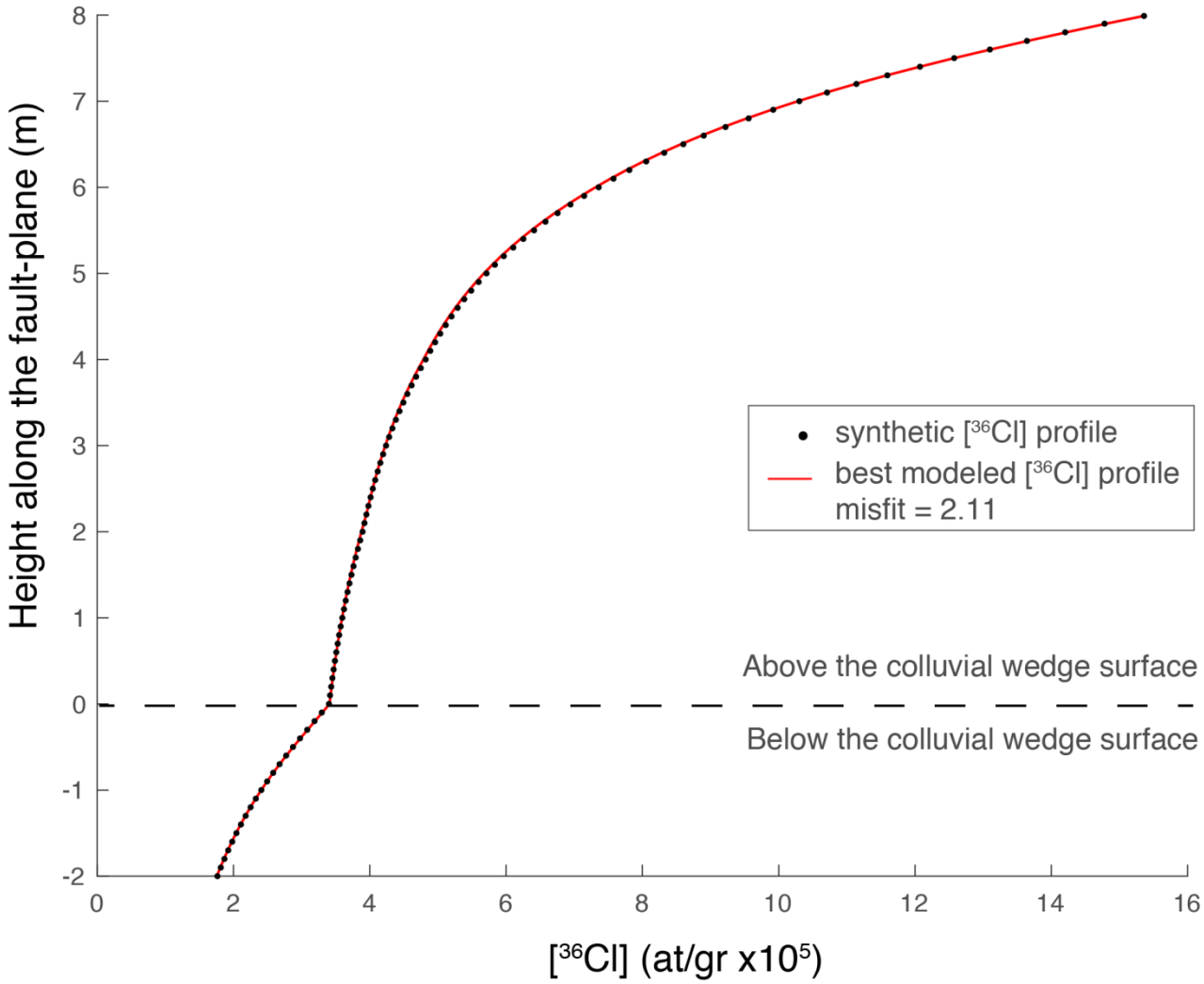

Figure B.6: Results inferred from the inversion of the synthetic [^{36}Cl] profile of a 8 m fault-plane. The synthetic scenario used for the inversion is composed of single cluster of 4 events at 4.5-6.0 ka, and a quiescence period between 30 and 6.0 ka. The synthetic [^{36}Cl] profile (black dots) is compared with the [^{36}Cl] profile of the best model (red line).

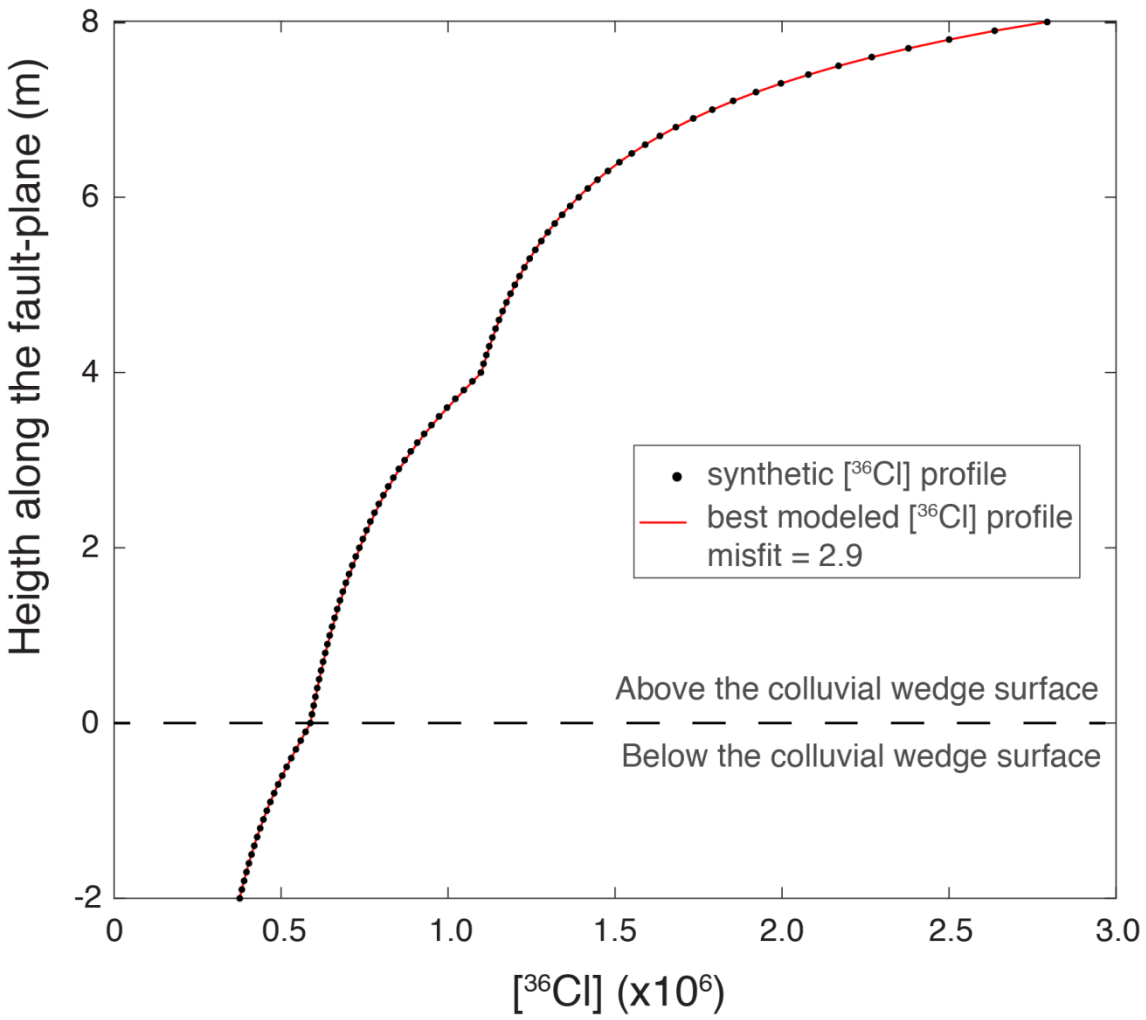

Figure B.7: Results inferred from the inversion of the synthetic [^{36}Cl] profile of a 8 m fault-plane, in the case of a slow-slipping fault. The synthetic scenario used for the inversion is composed of a cluster of 4 events at 5.0, 5.5, 15.0 and 15.5 ka, and a peri-glacial inheritance produced by a peri-glacial denudation of 30 m/Myr. The synthetic [^{36}Cl] profile (black dots) is compared with the [^{36}Cl] profile of the best model (red line, RMSw = 2.9).

Figure 1: Picture of the fault-plane exhumed during the 2016 Vettore earthquake in Central Italy (white part at the bottom of the scarp, around 2 m of displacement, see details in Perouse et al. 2018).

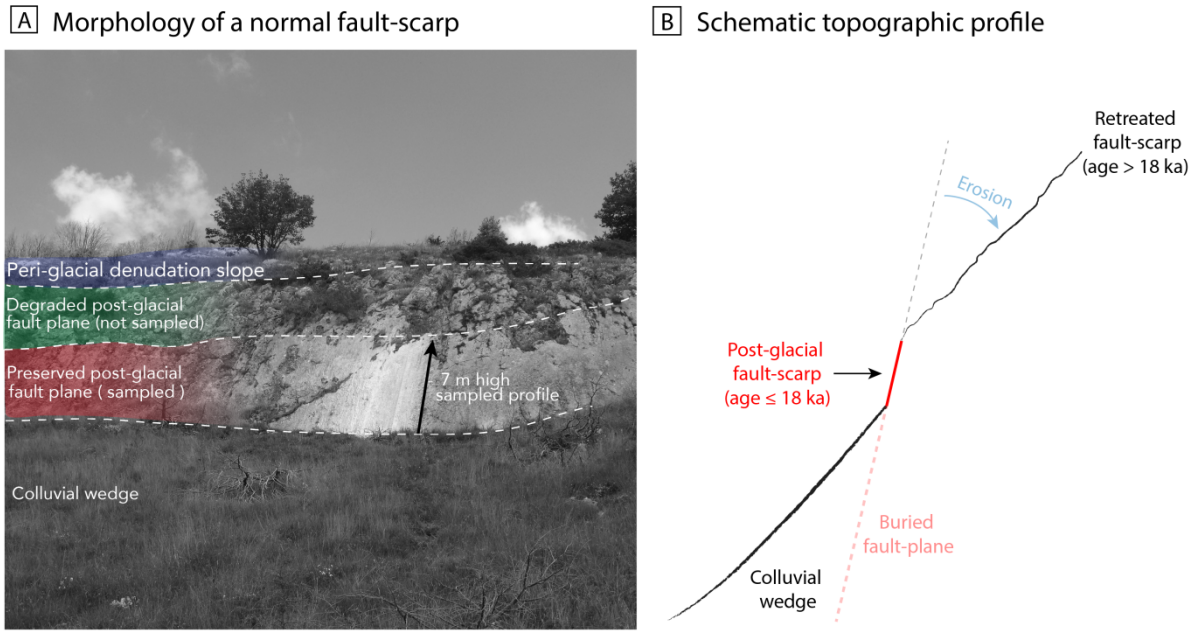

Figure 2: Example of a fault-scarp with A) 3 distinct zones: an upper peri-glacial denudation slope (blue area), the post glacial fault-scarp with a degraded upper zone not sampled (green area), and the 7 m high preserved zone, suitable for sampling (red area). B) Schematic topographic profile of a fault-scarp.

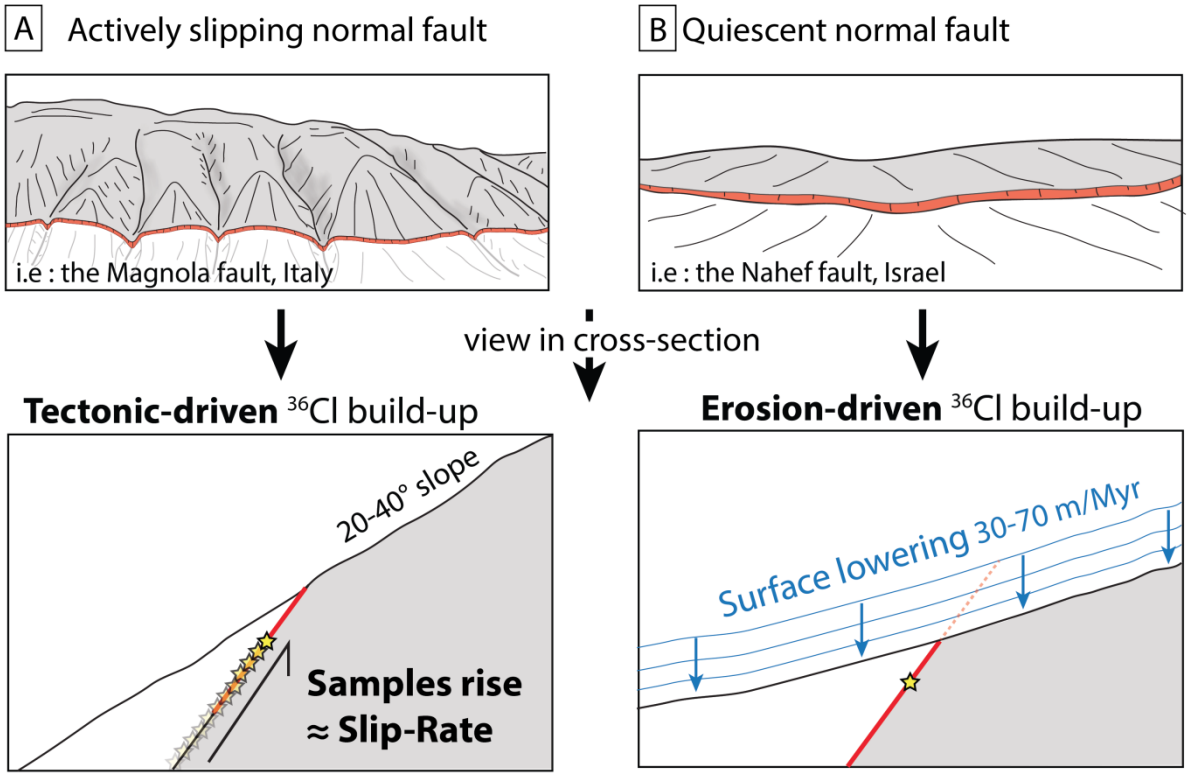

Figure 3: Processes that lead to the ^{36}Cl build-up in a fault-plane prior its post-glacial exhumation: (A) Case of an actively slipping normal faults as the Magnola fault (Palumbo et al. 2004) and (B) Case of a quiescent or very slowly slipping normal fault as the Nahef fault (Mitchell et al. 2001). The top panel illustrates the typical morphology associated with those normal faults, generally associated with a preserved post-glacial fault-scarp (in red). The bottom panel is a cross section of the fault-zone illustrating the process that makes the sample depth *z(t)* decreases over the time, during the peri-glacial period. The red line represents the fault-plane, and the star is the successive position of the sample over time along the fault-plane.

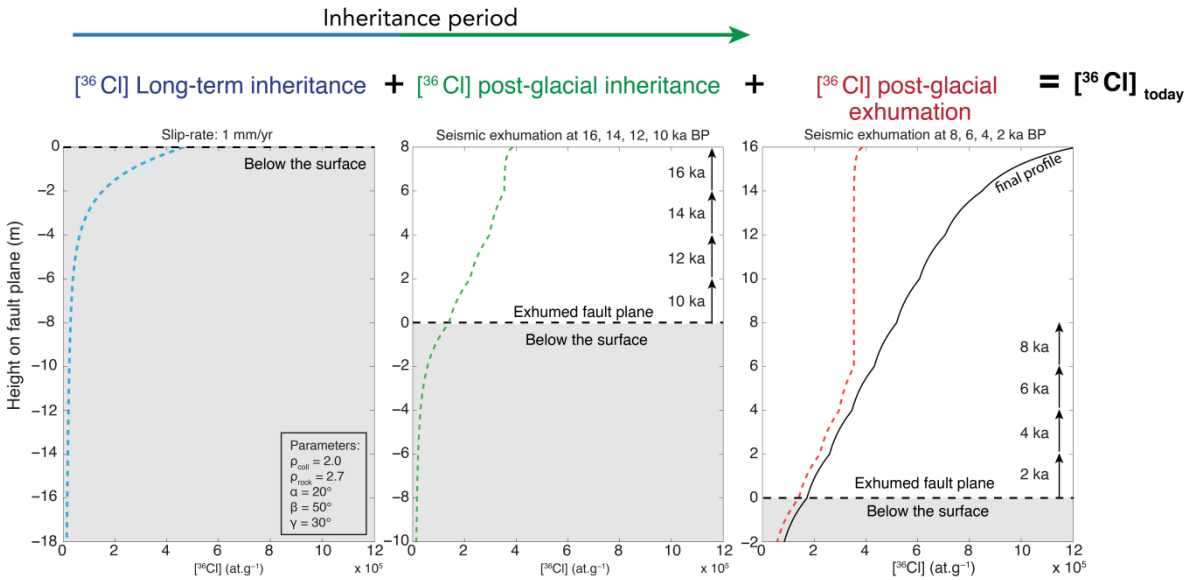

Figure 4: Deconvolution of the three ^{36}Cl uptake on a fault scarp: 1) during the long-term inheritance period (here slip-rate 1 mm/yr, left panel), 2) during the exhumation of the upper fault scarp portion, too eroded to be sampled, that we will called the post-glacial inheritance (here at 10, 12, 14 and 16 ka with 2 m of slip per event, central panel), and 3) during the exhumation of the preserved sampled fault-plane (called the post-glacial exhumation, here at 2, 4, 6 and 8 ka with a slip per event of 2 m, right panel). The dashed line represents the ^{36}Cl accumulated during the considered period, and the black line represent the final [^{36}Cl] profile.

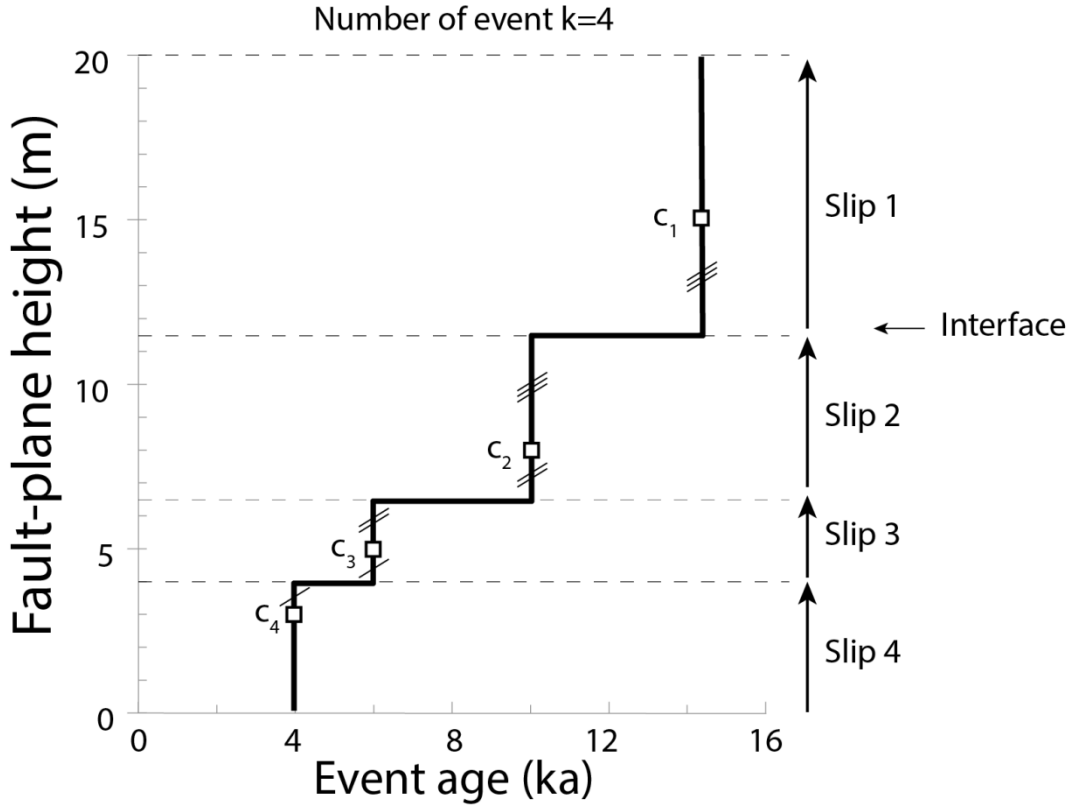

Figure 5: Each model is parameterized by a variable number of event *k* (here 4) that exhumed several portion *i* of the fault-plane, each portion of the fault-plane having an age a_i. The geometry of the exhumed portion of the fault-plane is described using Voronoi nuclei c_i (square). The vertical position(s) of the nuclei c_i determine the location of the interface(s) between each exhumed portion (dashed lines), defined as the equidistant between adjacent nuclei. The nuclei are thus not necessary in the middle of a portion. The slip s_i of each event *i* is obtained by the size of the exhumed portion. The black curve represents the slip over the time of the model.

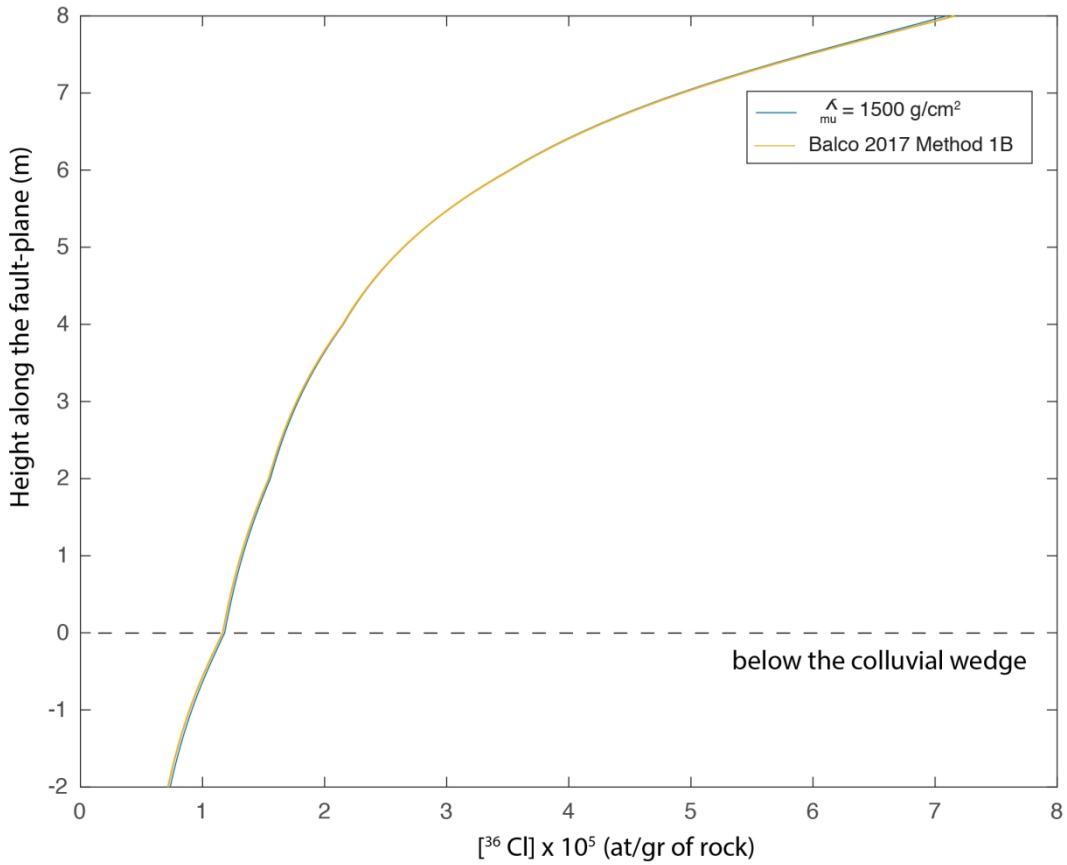

Figure 6: Comparison of two synthetic [^{36}Cl] profiles using 1) an attenuation length for the muons of 1500 g/cm2, 2) the Balco (2017) model (method 1B). The scenario used to generate the synthetic [^{36}Cl] profile is composed of a long-term inheritance of 300 kyr with a fault slip-rate of 1 mm/yr, a post-glacial inheritance corresponding to the sporadic exhumation of the upper fault-plane (8 m), and the exhumation of 8 m of the sampled fault-plane by 4 events of 2 m slip each.

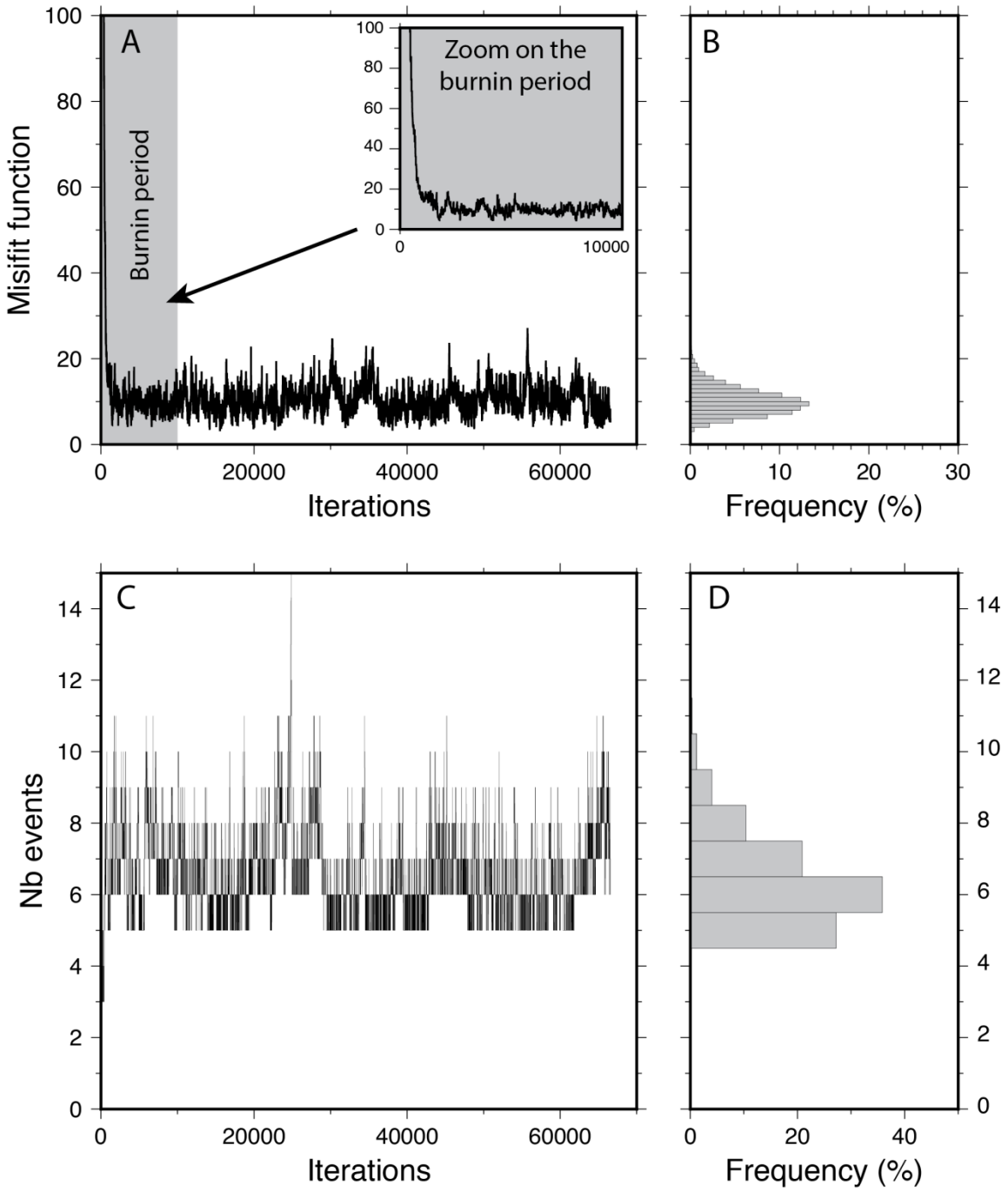

Figure 7: Inversion of a synthetic [^{36}Cl] profile previously generated by a long-term inheritance of 300 kyr with a fault slip-rate of 1 mm/yr, a post-glacial inheritance corresponding to the sporadic exhumation of the upper fault-plane (8 m), and the exhumation of 8 m of the sampled fault-plane by 4 events of 2 m slip each. A) Evolution of the misfit function over the iteration of the algorithm. The grey band corresponds to the burn' in period (discarded models for the statistical analysis). B) Histogram of the misfit values. C) Number of events over the iterations. D) Frequency of the number of events.

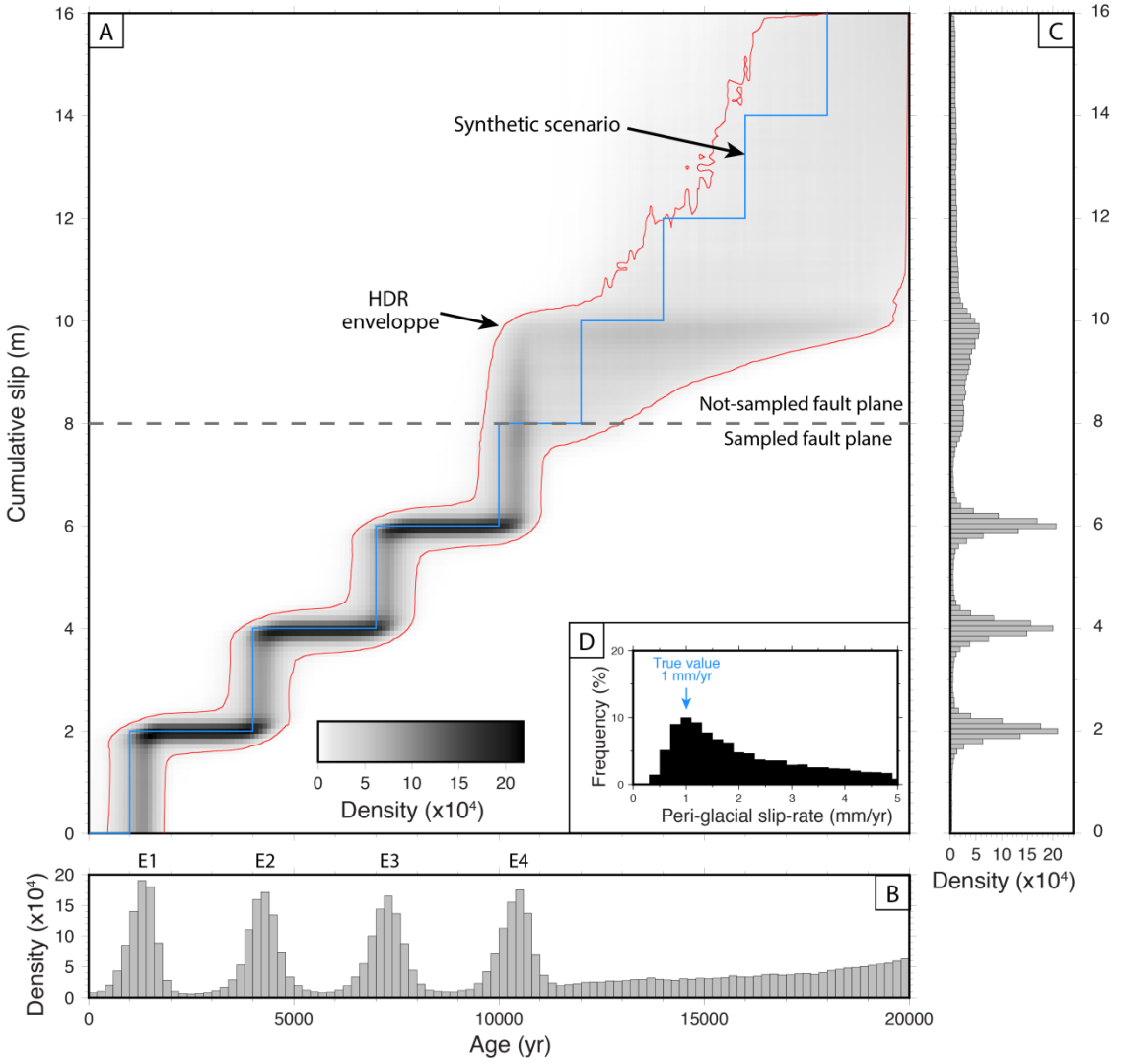

Figure 8: Results inferred from the inversion of the synthetic [^{36}Cl] profile of a fault-plane sampled up to 8 m. A) Density plot of the cumulative slip over time obtained from models of the rj-McMC chain (about 740 000 models), compared with the true scenario (blue). The highest density region (HDR), figured by the red envelop, includes the 95% most frequent models. B) Density distribution of event ages. C) Density distribution of the interfaces location between successive events along the fault-plane. D) Distribution of the yielded peri-glacial slip-rate.

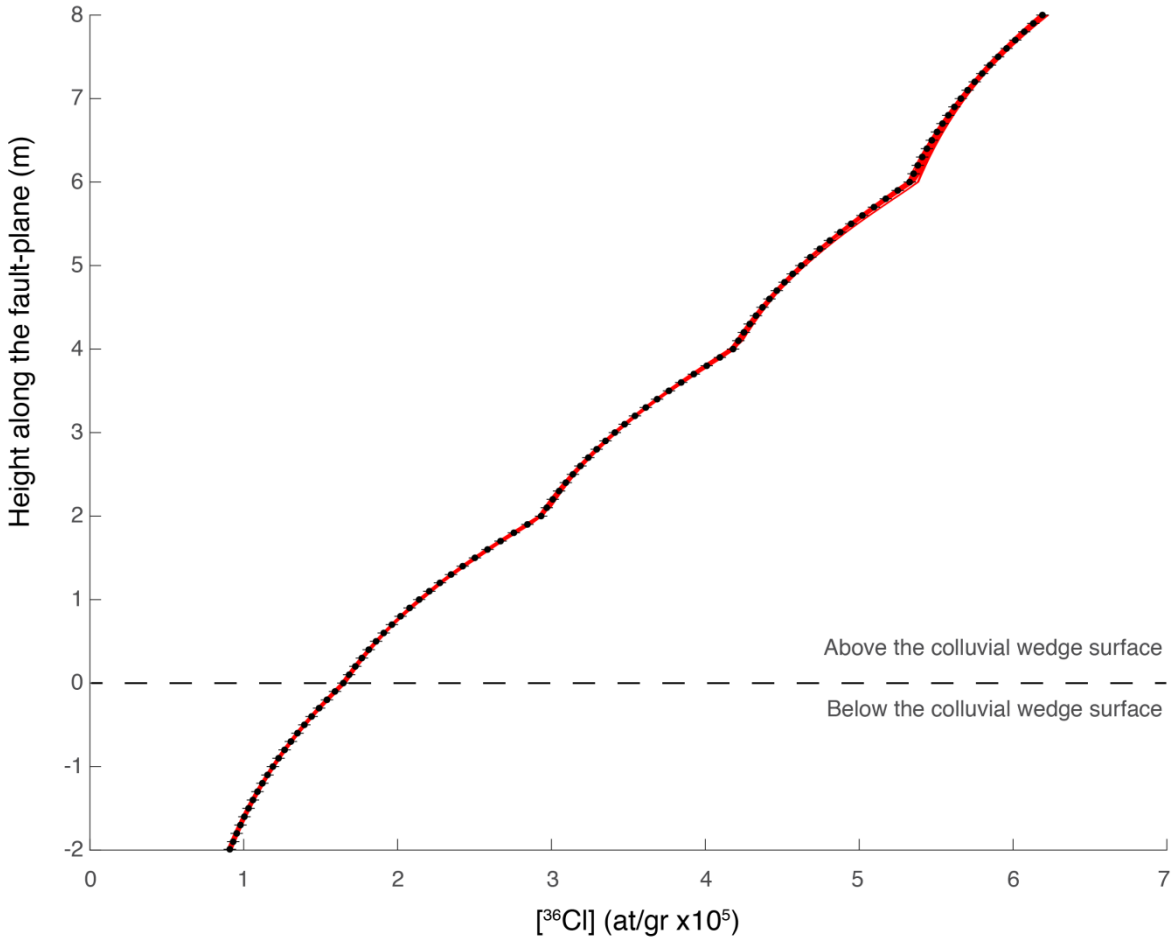

Figure 9: Comparison between modeled [^{36}Cl] profiles from the 100 best models obtained from the inversion (red lines), and the synthetic [^{36}Cl] profile (black dots with 2σ uncertainties).

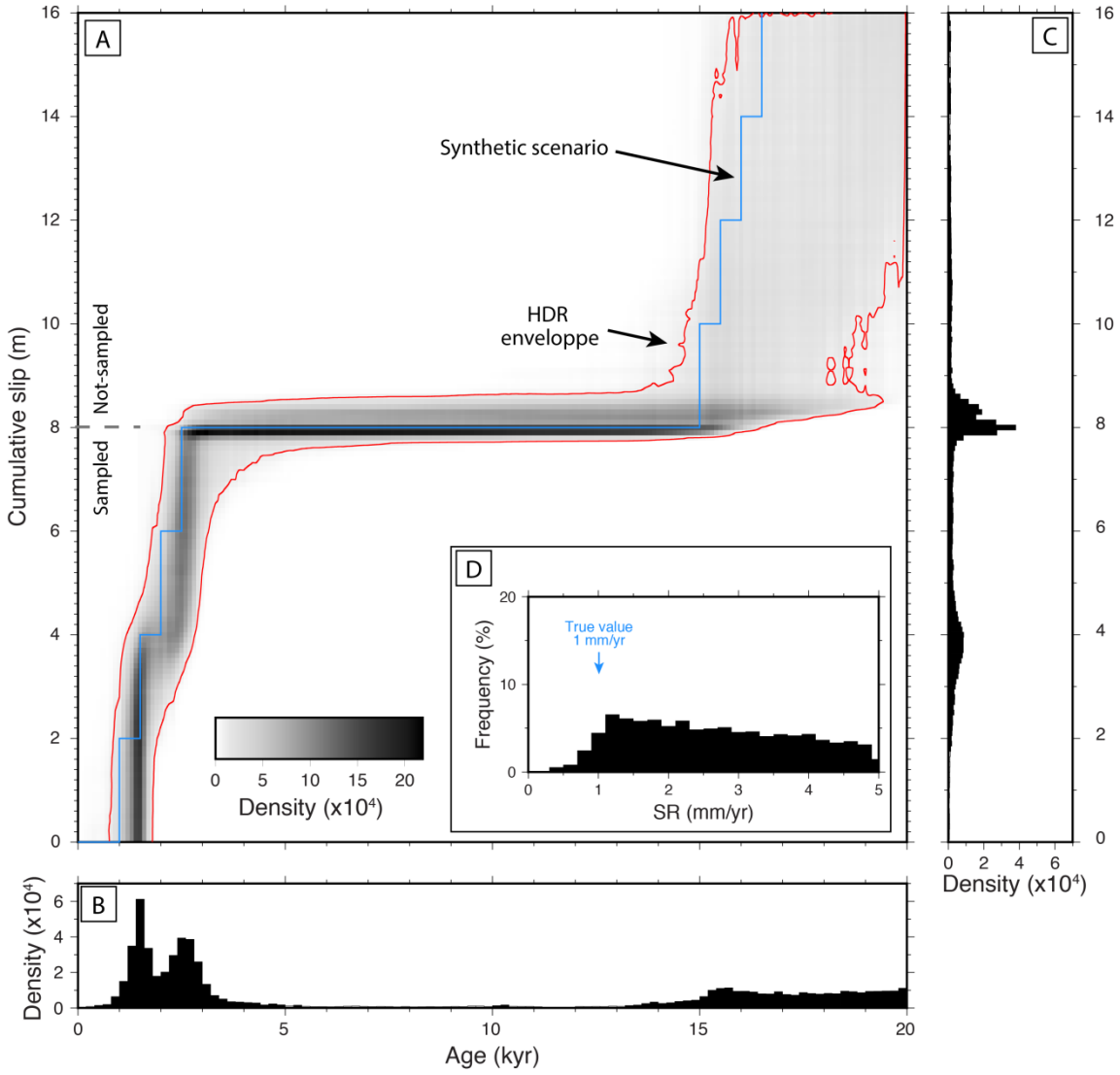

Figure 10: Results inferred from the inversion of the synthetic [^{36}Cl] profile of a fault-plane sampled up to 8 m. The synthetic scenario used for the inversion is composed of two clusters of 4 events at 1.0-2.5 ka and 15.5-16.5 ka. A) Density plot of the cumulative slip over time obtained from models of the rj-McMC chain (about 140 000 models), compared with the true scenario (blue). The highest density region (HDR), figured by the red envelop, includes the 95% most frequent models. B) Density distribution of event ages. C) Density distribution of the location of interfaces between the successive events along the fault-plane. D) Distribution of the peri-glacial slip-rate.

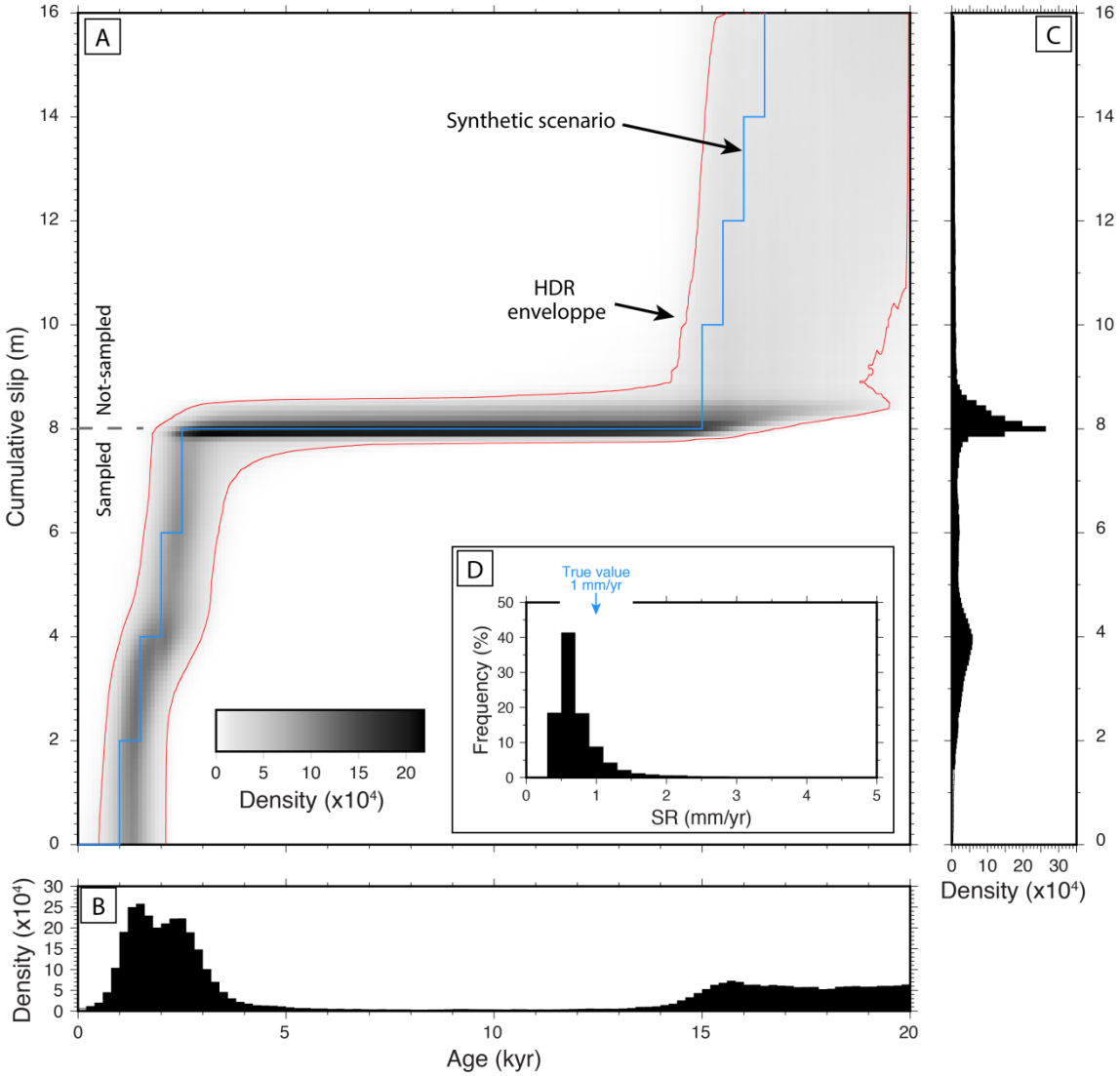

Figure 11: Results inferred from the inversion of the synthetic [^{36}Cl] profile of a fault-plane sampled up to 8 m. The synthetic scenario used for the inversion is composed of two cluster of 4 events at 1.0-2.5 ka and 15.5-16.5 ka, and a quiescence period between 30 and 16.5 ka. A) Density plot of the cumulative slip over the time obtain from models of the rj-McMC chain (about 140 000 models), compared with the synthetic scenario (blue). The highest density region (HDR), figured by the red envelop, includes the 95% most frequent models. B) Density distribution of event ages. C) Density distribution of the location of interfaces between the successive events along the fault-plane. D) Distribution of the peri-glacial slip-rate.

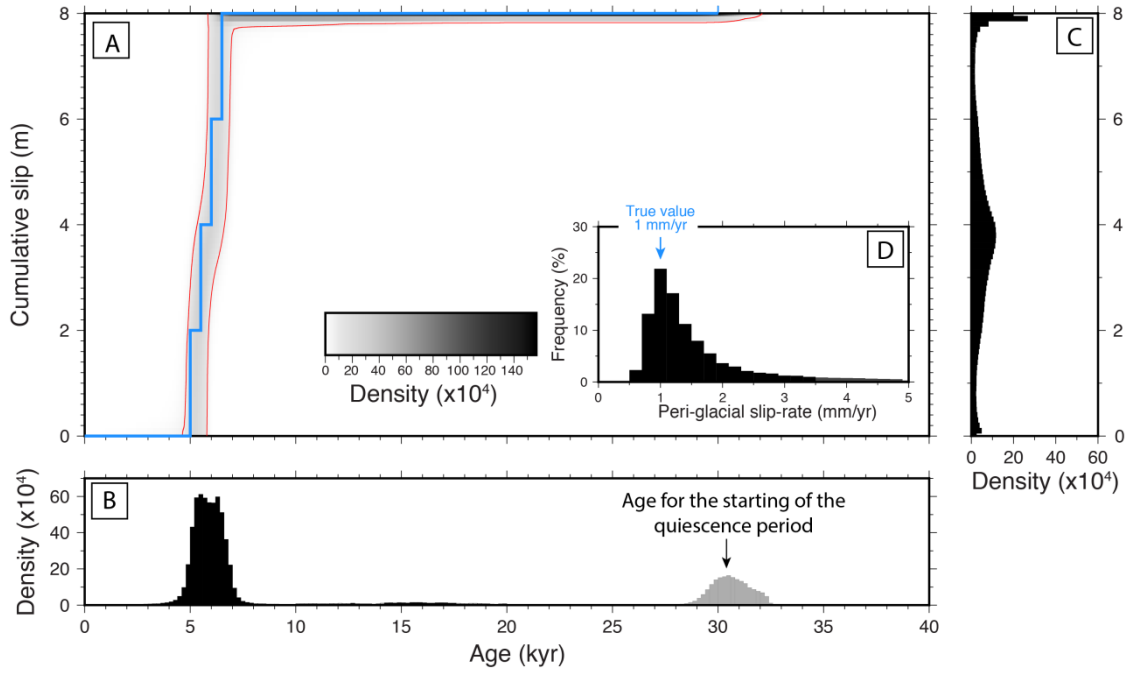

Figure 12: Results inferred from the inversion of the synthetic [^{36}Cl] profile of a 8m high fault-plane, sampled up to the top. The synthetic scenario used for the inversion is composed of a cluster of 4 events between 5.0 and 6.5 ka, and a quiescence period between 30 ka and 6.5 ka. A) Density plot of the cumulative slip over time obtained from models of the rj-McMC chain (about 190 000 models), compared with the true scenario (blue). The highest density region (HDR), figured by the red envelop, includes the 95% most frequent models. B) Density distribution of event ages in black, and of the starting of the quiescence period in grey. C) Density distribution of the location of interfaces between the successive events along the fault-plane. D) Distribution of the peri-glacial slip-rate, prior the quiescence period.

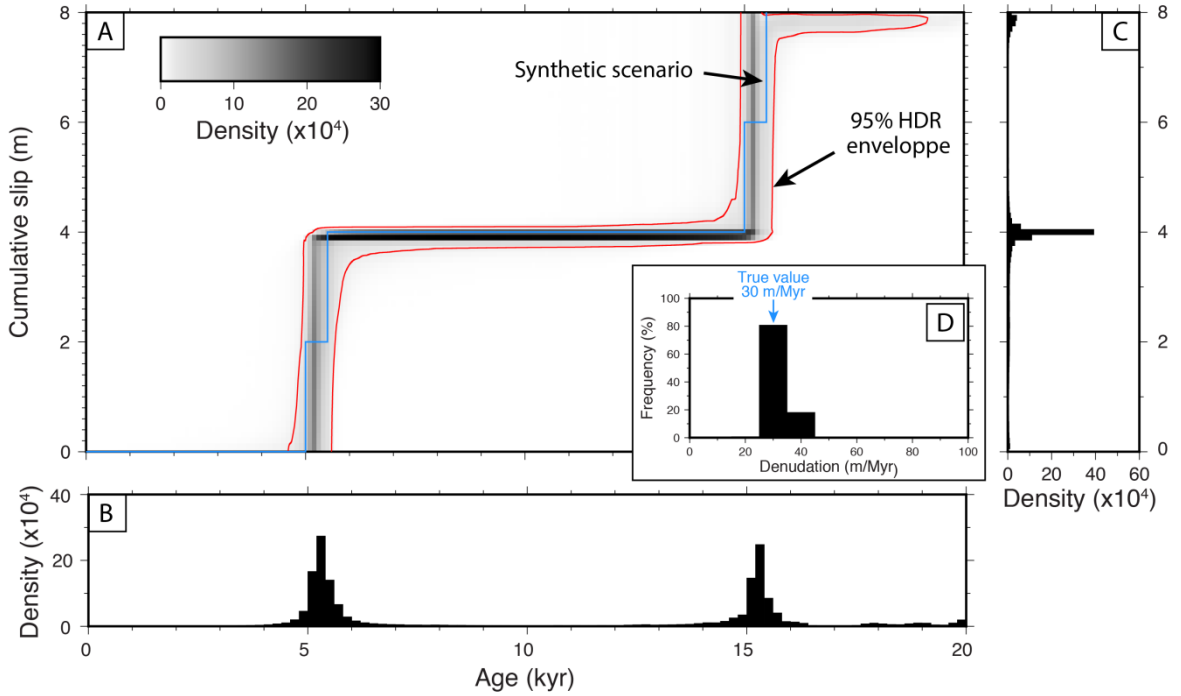

Figure 13: Case of a slow slipping fault, where the inherited ^{36}Cl contribution is directly controlled by the denudation rate that progressively lowers the surface of the whole scarp during peri-glacial times. Results inferred from the inversion of the synthetic [^{36}Cl] profile of an 8m high fault-plane, sampled up to the top. The true scenario used for the inversion is composed of a cluster of 4 events at 5.0, 5.5, 15.0 and 15.5 ka, and a peri-glacial inheritance produced by a peri-glacial denudation of 30 m/Myr. A) Density plot of the cumulative slip over the time obtain from models of the rj-McMC chain (about 560 000 models), compared with the true scenario (blue). The highest density region (HDR), figured by the red envelop, includes the 95% most frequent models. B) Density distribution of event ages in black, and of the starting of the quiescence period in grey. C) Density distribution of the location of interfaces between the successive events along the fault-plane. D) Distribution of the peri-glacial slip-rate, prior the quiescence period.

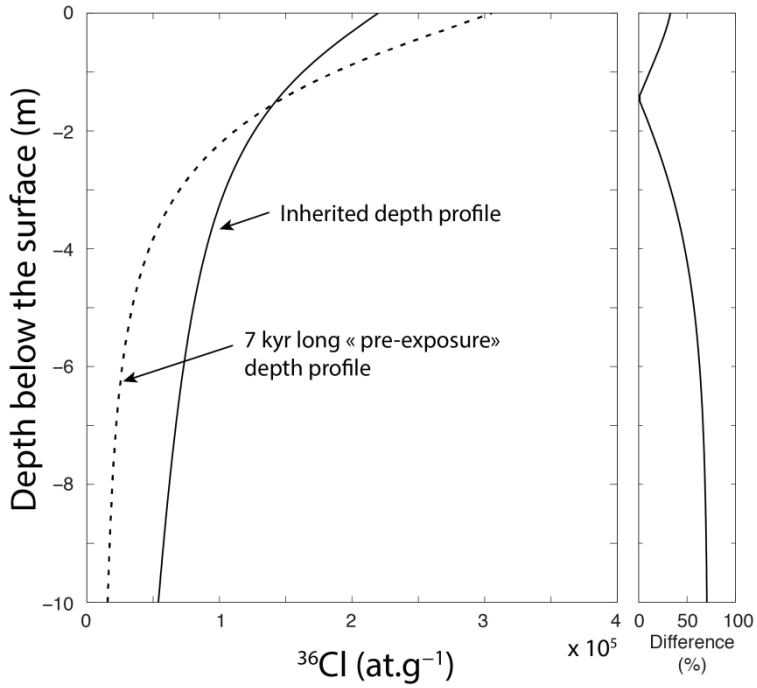

Figure 14: ^{36}Cl profiles as function of depth below the surface of the colluvial wedge. Dark line is scenario produced with a fault plane initially exposed at depth during 300 kyr with a fault slip-rate of 0.5 mm/yr and then exhumed by sporadic events during 10 kyr (8 m of total displacement). The dashed line is the ^{36}Cl profile derived from the same post-glacial exhumation but with no long-term inheritance and only considering a fixed amount of pre-exposure prior the post-glacial exhumation as done in Schlagenhauf et al. (2010) (here pre-exposure is 7 kyr). The right panel indicates the difference between the two curves.